AGU PUBLICATIONS

JGR

Journal of Geophysical Research: Oceans

RESEARCH ARTICLE

10.1002/2017JC012849

Special Section:
The Southern Ocean Carbon and Climate Observations and Modeling (SOCCOM) Project: Technologies, Methods, and Early Results

Key Points:
- Doubling of the atmospheric CO_2 levels leads to a 0.56°C warming for the Antarctic shelf region ocean in the GFDL CM2.6 climate model
- Heat advection across the shelf break is the primary driver of CO_2-forced shelf warming
- CO_2-forced shelf freshening influences both the magnitude and the location of shelf warming at depth

Supporting Information:
- Supporting Information S1

Correspondence to:
P. Goddard,
pgoddard@email.arizona.edu

Citation:
Goddard, P. B., Dufour, C. O., Yin, J., Griffies, S. M., & Winton, M. (2017). CO_2-induced ocean warming of the Antarctic continental shelf in an eddying global climate model. *Journal of Geophysical Research: Oceans*, *122*, 8079–8101. https://doi.org/10.1002/2017JC012849

Received 28 FEB 2017
Accepted 11 SEP 2017
Accepted article online 17 SEP 2017
Published online 25 OCT 2017

CO_2-Induced Ocean Warming of the Antarctic Continental Shelf in an Eddying Global Climate Model

Paul B. Goddard[1], Carolina O. Dufour[2,3], Jianjun Yin[1], Stephen M. Griffies[4], and Michael Winton[4]

[1]Department of Geosciences, University of Arizona, Tucson, AZ, USA, [2]Atmospheric and Oceanic Sciences Program, Princeton University, Princeton, NJ, USA, [3]Department of Atmospheric and Oceanic Science, McGill University, Montreal, QC, Canada, [4]Geophysical Fluid Dynamics Laboratory, NOAA, Princeton, NJ, USA

Abstract Ocean warming near the Antarctic ice shelves has critical implications for future ice sheet mass loss and global sea level rise. A global climate model with an eddying ocean is used to quantify the mechanisms contributing to ocean warming on the Antarctic continental shelf in an idealized $2xCO_2$ experiment. The results indicate that relatively large warm anomalies occur both in the upper 100 m and at depths above the shelf floor, which are controlled by different mechanisms. The near-surface ocean warming is primarily a response to enhanced onshore advective heat transport across the shelf break. The deep shelf warming is initiated by onshore intrusions of relatively warm Circumpolar Deep Water (CDW), in density classes that access the shelf, as well as the reduction of the vertical mixing of heat. CO_2-induced shelf freshening influences both warming mechanisms. The shelf freshening slows vertical mixing by limiting gravitational instabilities and the upward diffusion of heat associated with CDW, resulting in the buildup of heat at depth. Meanwhile, freshening near the shelf break enhances the lateral density gradient of the Antarctic Slope Front (ASF) and disconnect isopycnals between the shelf and CDW, making cross-ASF heat exchange more difficult. However, at several locations along the ASF, the cross-ASF heat transport is less inhibited and heat can move onshore. Once onshore, lateral and vertical heat advection work to disperse the heat anomalies across the shelf region. Understanding the inhomogeneous Antarctic shelf warming will lead to better projections of future ice sheet mass loss.

1. Introduction

The Antarctic ice sheet is the largest ice reservoir on Earth and the largest potential contributor to global sea level rise (Bamber et al., 2009; Lythe et al., 2001; Shepherd et al., 2004). Recent studies using observations and numerical models indicate that the ice sheet is losing mass at an increasing rate, contributing to present and future projections of global sea level rise (e.g., DeConto & Pollard, 2016; Pritchard et al., 2012; Rignot et al., 2008; Timmermann & Hellmer, 2013). Most of the land-based ice mass loss is a result of the melting or calving of ice shelves buttressing the ice sheet (Depoorter et al., 2013). Ice shelf basal melt mainly results from intrusion of relatively warm and saline Circumpolar Deep Water (CDW) onto the continental shelf (e.g., Cook et al., 2016; Jenkins et al., 2016; Obase et al., 2017; Rignot & Jacobs, 2002). Typically, CDW is characterized by temperatures about 3°C–4°C above the seawater freezing point (Whitworth et al., 1998). Where CDW is able to approach the ice shelves from below, it efficiently melts ice shelves, reducing their buttressing effect for the inland ice streams and prompts accelerated land-to-sea ice motion (Dupont & Alley, 2005). Some of the most vulnerable ice shelves are located along the coast of the Antarctic Peninsula and in the Bellingshausen and Amundsen Seas (e.g., Christie et al., 2016; Jacobs et al., 1996; Martinson et al., 2008; Payne et al., 2004) and near the Totten Glacier on the Sabrina Coast in East Antarctica (Greenbaum et al., 2015).

Usually, CDW is kept off the Antarctic shelf break and from the cold shelf waters by the Antarctic Slope Front (ASF). However, the ASF is largely absent near the shelf break of the western Antarctic Peninsula and in the Bellingshausen and Amundsen Seas (Gill, 1973; Jacobs, 1991). The ASF is associated with steep isopycnals which tilt down toward the continental slope and limit cross-shelf-break heat transport, thereby serving as a natural barrier between CDW and the Antarctic ice shelves (Whitworth et al., 1998). The steep tilt of isopycnals, mainly resulting from Ekman downwelling from the coastal Easterlies, can create lateral density gradients across the ASF. Along the continental slope, some isopycnals link CDW to the shelf (see Stewart & Thompson, 2016, Figure 2). This connection of isopycnals provides a key pathway for heat exchange across the shelf break.

Recent observations and model-based studies suggest that mesoscale eddies contribute significantly to onshore heat transport across the ASF (e.g., Hattermann et al., 2014; Nøst et al., 2011; Stewart & Thompson, 2015). Occurring preferentially along isopycnals, this eddy heat transport is sensitive to local topographic and isopycnals slopes (for details, see Isachsen, 2011). For example, a shallow continental shelf break or steep continental slope can reduce cross-ASF connecting isopycnals and therefore restrict heat exchange across the ASF (Hattermann et al., 2014). Conversely, projected weakening of the coastal Easterly wind stress may lead to a flattening and shoaling of the isopycnals crossing the ASF, resulting in enhanced cross-ASF eddy heat transport (Spence et al., 2014). Furthermore, studies show that increasing freshwater input from ice sheet basal melting into the shelf waters (Nøst et al., 2011) or increasing the shelf salinity from polynya brine rejection (Stewart & Thompson, 2015, 2016) can enhance cross-ASF onshore eddy heat transport. Through seemingly opposite forcings, these studies both show increased available potential energy on the shelf which is released through more onshore eddy heat transport.

Previous modeling studies have investigated the mechanisms driving heat transport toward Antarctica's ice shelves (e.g., Dinniman et al., 2011; Hattermann et al., 2014; Nøst et al., 2011; Stewart & Thompson, 2015, 2016; St-Laurent et al., 2013). These studies use fine-resolution ocean models and are conducted at regional scales or with an idealized model domain. Therefore, results from sensitivity experiments may lack feedbacks otherwise represented in fully coupled global climate models. On the other hand, previous projections of the ocean warming around the Antarctic ice sheet employed global coupled climate models with $\sim 1°$ resolution for the ocean model (Yin et al., 2011). Climate models at this resolution represent large-scale features well but are unable to properly capture the narrow ASF, Antarctic Slope Current, and other important shelf and coastal processes near the Antarctic ice sheet (supporting information Figure S3a; Heuze et al., 2013). Recently, the advent of fine-resolution global ocean-sea ice models and fully coupled climate models have allowed the investigation of ocean warming along the Antarctic coasts (Spence et al., 2017) and further study the role of eddies in water mass transformation and overturning circulation off Antarctica (Newsom et al., 2016).

Here we use a 0.1° horizontal resolution fully coupled global climate model with an active mesoscale eddying ocean component to study ocean warming of the Antarctic continental shelf in an idealized doubling of CO_2 ($2xCO_2$) experiment. The model's representation of dynamic feedbacks between the eddying ocean and other climate components allows for a comprehensive analysis of the decadal response of the Antarctic shelf region to CO_2 forcing. Aiming for a detailed heat budget analysis, we quantify the ocean advective heat transport across the ASF and its decomposition into mean and eddy components. We compare this heat transport with surface heat fluxes, vertical heat advection, and vertical mixing of heat in both the control run and the CO_2 experiment. We find a strong relationship between CO_2-forced shelf freshening and the location and magnitude of positive temperature anomalies. We show that shelf freshening strengthens the ASF and reduces vertical mixing of heat. Through these changes, shelf freshening becomes an important mechanism for controlling onshore heat transport and the spatial distribution and magnitude of positive temperature anomalies on the shelf. Our analyses contribute new understanding to the causes of Antarctic shelf ocean warming. The paper is organized as follows: section 2 describes the model and experiment, section 3 presents the simulation results and the underlying mechanisms, section 4 includes our discussion, and section 5 contains our conclusions.

2. Model and Methods

2.1. Model and Simulations

In the present study, we use the GFDL CM2.6 global coupled climate model (Delworth et al., 2012; Griffies et al., 2015). The ocean component is based on the Modular Ocean Model Version 5 (MOM5; Griffies, 2012). MOM5 utilizes the z* vertical coordinate and has 50 vertical levels, increasing from a thickness of 10 m near the surface to 210 m at depth. The atmospheric model has a horizontal resolution of about 50 km with 32 vertical levels. CM2.6 employs a dynamical sea ice model with three vertical layers, one snow and two ice, plus five ice thickness classifications (Delworth et al., 2006). The model neither resolves ice shelf cavities nor is coupled to a dynamic ice sheet model. However, surface runoff and calving are included and fluctuate to maintain mass balance on the Antarctic continent. For a detailed description of CM2.6, the reader is referred to Delworth et al. (2012) and Griffies et al. (2015).

The ocean component of CM2.6 has a horizontal resolution of 0.1° using a Mercator projection, which yields roughly 4–6 km grid spacing along the ASF. Notably, no mesoscale eddy transport parameterization is used; however, we make use of a mixed layer submesoscale eddy parameterization (Fox-Kemper et al., 2011). Furthermore, overflow processes are not parameterized. Lastly, tides are not represented in CM2.6, though studies show tides play a role in the structure of the ASF (e.g., Flexas et al., 2015).

CM2.6 exhibits a rich eddy field along a well-defined ASF as well as high eddy kinetic energy along the Antarctic Slope Current (Delworth et al., 2012). It should be noted that an ocean grid size of about 1 km is necessary to resolve the full mesoscale eddy field near the Antarctic shelf, as the baroclinic Rossby deformation radius is about 4 km (Hallberg, 2013; Stewart & Thompson, 2015; St-Laurent et al., 2013). Thus, the horizontal resolution of CM2.6 likely underrepresents mesoscale eddy activity near the ASF. The reduced mesoscale eddy activity near the shelf break may explain the strong ASF in CM2.6 when compared to the World Ocean Circulation Experiment (WOCE) transects (supporting information Figure S4; Sparrow et al., 2011). With insufficient mesoscale eddy activity, the ASF isopycnals remain steep and limit exchanges of heat and salt across the shelf break (Isachsen, 2011; Stewart & Thompson, 2015). This model characteristic leads to a cold temperature bias on the western Antarctic Peninsula shelf (67°S) where the strong ASF prevents CDW from reaching the shelf in CM2.6 (supporting information Figure S4). In section 4, we discuss potential caveats to our results regarding this model bias. Nonetheless, the model's fine-scale bathymetry and rich eddy field allow for a reasonable representation of the Antarctic shelves and associated circulation.

A 200 year control simulation is carried out with CM2.6 under 1860-preindustrial conditions. An idealized 2xCO_2 experiment branches from the control simulation at model year 121, wherein the atmospheric CO_2 concentration increases by 1% per year until year 200. A CO_2 doubling is reached after 70 years ($\sim$570 ppm). The CO_2 concentration is roughly equivalent to RCP6.0 at year 2080 or RCP8.5 at year 2055 (Meinshausen et al., 2011; van Vuuren et al., 2011). For simplification, year 1 hereinafter refers to the first year of the 2xCO_2 experiment.

2.2. Analysis Regions and Time Period

In this study, the Antarctic shelf region is defined as the ocean region shoreward of the 1000 m isobath (Figure 1a, black contour). In addition to closely following the Antarctic Slope Current (supporting information Figure S3b), the 1,000 m isobath closely follows the barotropic transport (supporting information Figure S3c). In the absence of friction, large-scale barotropic flow is constrained to follow contours of constant planetary geostrophic potential vorticity, f/h, with f the Coriolis parameter and h the bottom depth. Given that the flow on the Antarctic continental shelf has a nontrivial barotropic component, the topography strongly constrains the flow (e.g., Rintoul et al., 2013). Consequently, the time mean depth integrated flow closely follows isobaths (since f does not change much around the continent). Given that volume transport across the 1,000 m isobath is minimal (see section 2.3), the depth integrated heat transport across the 1,000 m isobath is roughly independent of the chosen reference temperature. We note that during the summer season, the depth integrated flow deviates from the 1,000 m isobath near the western Antarctic Peninsula. Significant flows can navigate the complex fjords and islands of the peninsula in the absence of sea ice, with friction breaking the constraints of potential vorticity conservation. Nonetheless, we choose a rigid definition of the ASF, the 1,000 m isobath, given that the ASF is well constrained by bathymetry and closely follows the Antarctic Slope Current.

Along the circumpolar 1,000 m isobath, we define the ASF "wall" as a virtual line extending vertically from the surface to the seafloor. To study spatial variability of ocean warming, we divide the Antarctic shelf region into six subdomains: western Peninsula, Weddell Sea, western East Antarctica, eastern East Antarctica, Ross Sea, and Amundsen and Bellingshausen Seas (Figure 1a). We perform a detailed heat budget analysis for the whole shelf region as well as for the six subdomains.

To evaluate the climate response to increased atmospheric CO_2, we compute the difference between annual mean model output of the control and CO_2-forced simulations over a 19 year period (years 62–80, with this period referring to years after the CO_2-forced simulation splits from the control). Starting at year 62, a strong polynya develops in the Weddell Sea, north of our Weddell Sea subdomain, in both the control

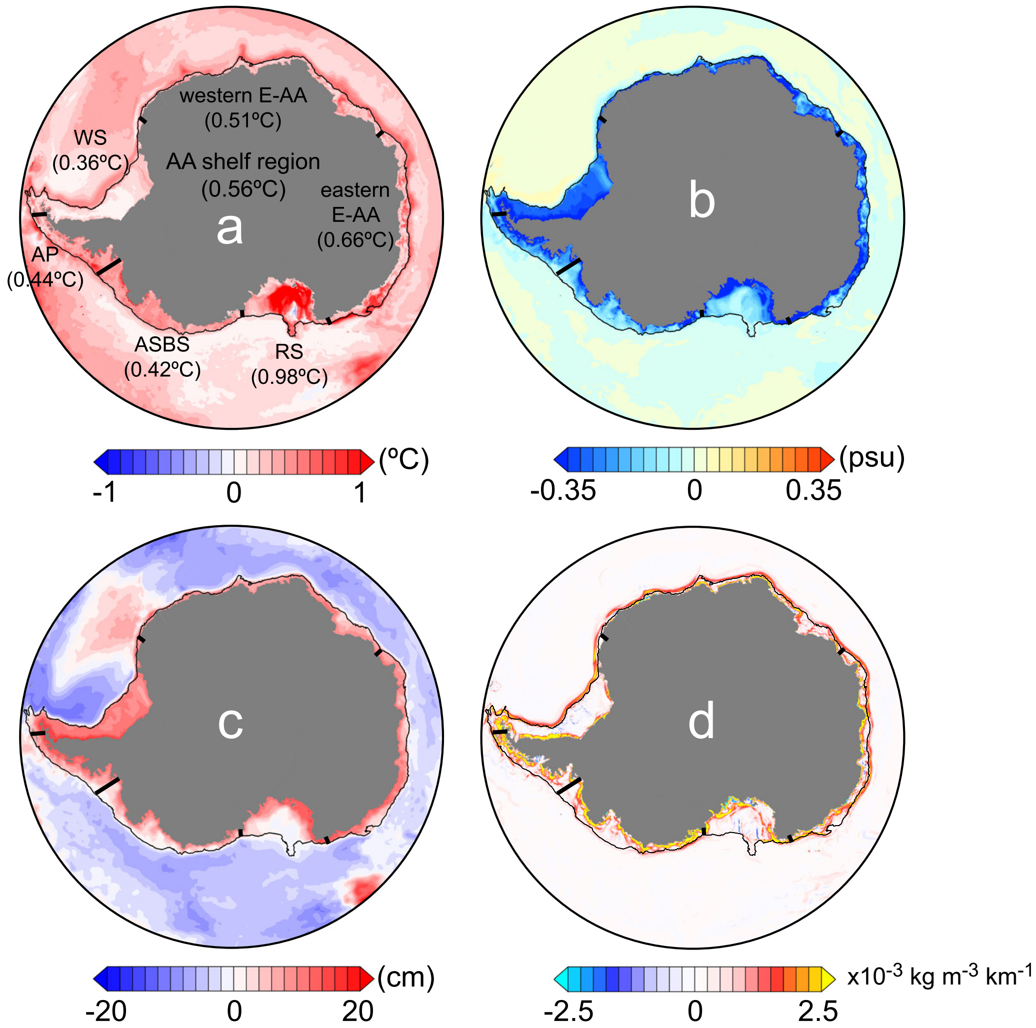

Figure 1. CO_2-forced Antarctic shelf region warming, freshening, dynamic sea level change, and lateral density gradient change for 0–1,000 m, averaged during years 62–80 (°C, psu, cm, x10^{-3} kg m^{-3} km^{-1}). (a) The 0–1,000 m mean temperature anomalies with listed volume-averaged temperature anomalies for the Antarctic shelf region and each subdomain (clockwise from the top: western East-Antarctic, eastern East Antarctic, Ross Sea, Amundsen and Bellingshausen Seas, western Antarctic Peninsula, and Weddell Sea), (b) salinity anomalies, (c) dynamic sea level change (global mean change is removed), and (d), lateral density gradient change. The lateral density gradient is the magnitude of the x and y centered derivative for each grid cell. Thin black contour is the 1,000 m isobath and location of the ASF "wall." Thick black lines denote boundary between subdomains.

and CO_2-forced simulations of CM2.6 (Dufour et al., 2017). Taking the difference between the two simulations allows us to remove most effects of the formation of the polynya on cross-ASF heat transport near the Weddell Sea shelf break (see supporting information Text and supporting information Figures S1 and S2 illustrating the minimal effect of the polynyas).

2.3. Heat and Volume Transport Across the ASF

Meridional and zonal advective fluxes of temperature and volume are integrated along the discretized front of the ASF "wall" (see Dufour et al., 2015, Appendix B). The transport is calculated at each model level (0–1,000 m depth) and each latitude-longitude coordinate along the 1,000 m isobath contour (denoted by "S"):

$$\Phi = \rho_0 \int_S C\, \boldsymbol{u} \cdot \hat{\boldsymbol{n}}\, dl\, dz, \quad (1)$$

where Φ is the tracer transport, ρ_0 is the reference density (1,035 kg m^{-3}), C is the tracer concentration, $\boldsymbol{u}$ is the horizontal velocity vector, $\hat{\boldsymbol{n}}$ is the normal vector along the "wall" pointing shoreward, dl are the line segments along the "wall," and dz is the model grid cell thickness. The tracer concentration, C is set to unity to compute volume transport in Sv.

Ocean temperature in °C becomes negative near Antarctica. We thus choose to reference temperature to the seawater freezing point calculated from the thermodynamic equation of seawater, 2010 (TEOS-10; IOC et al., 2010). Using the freezing point as a reference temperature ensures that volume and heat transport are in the same direction, and it provides a measure of the melt potential for the water reaching the ice shelves. This melt potential heat transport arises by setting

$$C = C_p(\theta - \theta_f), \tag{2}$$

where $C_p = 3{,}992.1$ J kg^{-1} K^{-1} is the seawater heat capacity and θ_f is the seawater freezing temperature. In the ocean, the freezing temperature is a function of salinity and pressure, with this dependence of importance to determine the ability of seawater to melt the ice shelf. However, C is not a conservative quantity when the melting temperature is a function of pressure. Hence, as an approximation, we use a constant freezing temperature $\theta_f = -2.69$°C, which is the minimum freezing temperature found at the ASF "wall" in our simulations. Additionally, we did not save the quantity $(\theta - \theta_f)$ during model integrations. Thus, while serving its primary role of ensuring that the volume and heat transports are in the same direction, our use of the minimum freezing temperature in equation (2) provides an upper bound to the true melting heat potential.

Following the methods described in Griffies et al. (2015) and Dufour et al. (2015), we decompose the total volume and heat transport into its time mean and transient eddy component for years 62–80. In the CM2.6 simulations, we saved the monthly mean of the zonal and meridional advective fluxes (Φ_{total}) which are accumulated at each model time step. The time mean component (Φ_{mean}) is calculated offline based on the 19 year monthly climatology of ocean velocity, temperature, and ocean layer thickness. The eddy component is the difference between the total component and mean component.

$$\Phi_{eddy} = \Phi_{total} - \Phi_{mean}. \tag{3}$$

Thus, the eddy component includes mesoscale eddies and other features contributing to interannual fluctuations of heat and volume transport across the ASF, while the time mean component captures the climatological monthly cycle over the 19 years.

2.4. Analysis Methods for Heat Budget

For the entire Antarctic shelf region ocean, the heat budget is primarily composed of surface heat fluxes and ocean advective heat transport across the ASF (Griffies, 2012):

$$\partial_t\left(\sum_k C_p\theta\rho_0 \mathrm{d}z\right) = -\nabla\cdot\left(\sum_k \left(C_p\rho_0\mathbf{u}\theta \mathrm{d}z + C_p\rho_0\mathbf{F}\mathrm{d}z\right)\right) + Q, \tag{4}$$

where net heat tendency on the left-hand side equals the sum of two terms on the right: the convergence of resolved and parameterized ocean heat transport ($C_p\rho_0\mathbf{u}\theta\mathrm{d}z$ and $C_p\rho_0\mathbf{F}\mathrm{d}z$, respectively), and the net surface heat flux (Q).

The convergence of ocean heat transport is the sum of the convergence of resolved lateral and vertical advective fluxes and the convergence of advective fluxes from the submesoscale eddy parameterization (Fox-Kemper et al., 2011). The net downward surface heat flux (Q) is the sum of

$$\text{radiative fluxes} = Q_s + Q_l, \tag{5}$$

$$\text{turbulent fluxes} = Q_h + Q_e + Q_{mc} + Q_{mp}, \tag{6}$$

$$\text{mass heat fluxes} = Q_c + Q_r + Q_{pme}, \tag{7}$$

where Q_s is shortwave radiation, Q_l is longwave radiation, Q_h is sensible heat, Q_e is latent heat of evaporation, Q_{mc} is heat to melt calved ice, Q_{mp} is heat to melt frozen precipitation, Q_c is heat flux at ocean surface from calving ice, Q_r is heat flux at ocean surface from runoff, and Q_{pme} is heat flux from precipitation minus evaporation transfer of water across the ocean surface.

Several terms work to redistribute heat in the vertical but vanish when integrated over the full water column, including vertical advection, penetrative heating from shortwave radiation, vertical diffusion, and the nonlocal heat redistribution from the KPP boundary layer parameterization (Large et al., 1994). The sum of the latter two terms measures the net vertical mixing of heat within a water column. Lastly, other negligible terms are not included in the equations above but are kept as part of our analysis to ensure heat budgets close to within computational roundoff.

3. Results

3.1. Antarctic Shelf Region Warming and Freshening

The volume-averaged ocean temperature of the Antarctic shelf region increases by 0.56°C in CM2.6 during years 62–80 of the 2xCO_2 experiment compared to the control simulation (Figure 1a). The warming in the six subdomains ranges from 0.36°C to 0.98°C, with the Ross Sea exhibiting the largest warming magnitude and the Weddell Sea the smallest. Furthermore, the spatial variation of the 0–1,000 m temperature anomalies closely resembles the warm anomalies at depth rather than near the surface. Near the surface, temperature anomalies are more spatially uniform except for larger warming near the western Antarctic Peninsula and Bellingshausen Sea (supporting information Figure S5).

Meanwhile, the Antarctic shelf region freshens during the 2xCO_2 experiment (Figure 1b). The shelf region freshening is mainly caused by increased precipitation, sea ice melt, and increased runoff/calving (supporting information Figure S6). The salinity anomalies penetrate downward with time and can reach depths greater than 500 m, most notably in the Weddell Sea (Figure 1b and supporting information Figure S5). The freshening anomaly reduces the volume-averaged salinity of the 0–1,000 m shelf region by 0.14 psu. As a response to the ocean warming and freshening, the dynamic sea level in the shelf region rises by up to 20 cm (Figure 1c). The halosteric component is the largest contributor to this dynamic sea level rise.

Figure 2 illustrates the transient warming pattern as a function of depth. In each subdomain, the surface warming gradually penetrates downward to ~100 m by year 80. By contrast, the deep warming begins near the shelf floor and shows a general upward propagation with time. The onset of the temperature anomalies varies by subdomain. In general, the upper and deeper temperature anomalies remain positive after year ~30 and ~45, respectively. In the following sections, we will investigate the mechanisms behind the different warming patterns at different depths and across the subdomains.

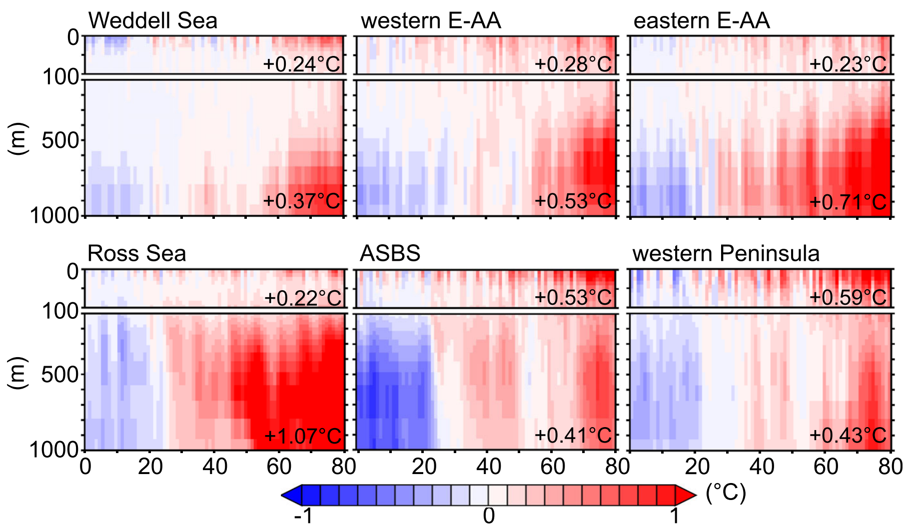

Figure 2. Model layer mean potential temperature anomalies at depth for CO_2-forced (years 1–80) minus years 62–80 average of the control simulation for each subdomain. Top 100 m is enlarged to show details. Listed are the volume-averaged temperature anomalies for years 62–80 for the top 100 m and the 100–1,000 m depth range.

3.2. The 0–100 m Warming and Heat Budget

For the 0–100 m depth range, the volume-averaged Antarctic shelf region temperature increases by 0.33°C. The western Peninsula and Amundsen and Bellingshausen Seas (ASBS) subdomains simulate the largest warming, with each warming by ~0.56°C (Figure 2). In contrast, the other four subdomains only warm by ~0.25°C. The temperature increase over the shelf region results from a heating of +0.4 TW (Figure 3a, equation (4)). Net surface heating, ocean lateral and vertical advective heating, and vertical mixing of heat regulate temperature anomalies in the top 100 m.

3.2.1. The 0–100 m Antarctic Shelf Region Net Surface Heat Flux

The net surface heat flux consists of multiple heat fluxes between the ocean and atmosphere as well as heat exchanges between the surface ocean and sea ice, calving, runoff, and precipitation, among other terms (equations (5)–(7)). All of the major surface boundary heat fluxes are enhanced under CO_2 forcing (Figure 3b). Due to a near-surface atmospheric warming of 2.8°C over the Antarctic shelf region and surface ocean warming, sea ice extent in the Antarctic shelf region substantially decreases during the austral summer and early autumn (supporting information Figure S7). Thus, more shortwave radiation penetrates into the ocean. This positive feedback works to extend the sea ice minimum season. The more expansive ice-free region permits more evaporative cooling and a larger ocean-to-atmosphere heat flux via longwave radiation and sensible heat loss. Additionally, there are small increases in ocean heat loss due to melting calved ice and frozen precipitation. The net response of the air-sea heat exchange is an increase in surface ocean heat loss (6.1 TW, or by 25%). Note, the surface heat flux anomalies show clear spatial variations. For example, the western Peninsula and Ross Sea subdomains show reduced ocean-to-atmosphere heat flux.

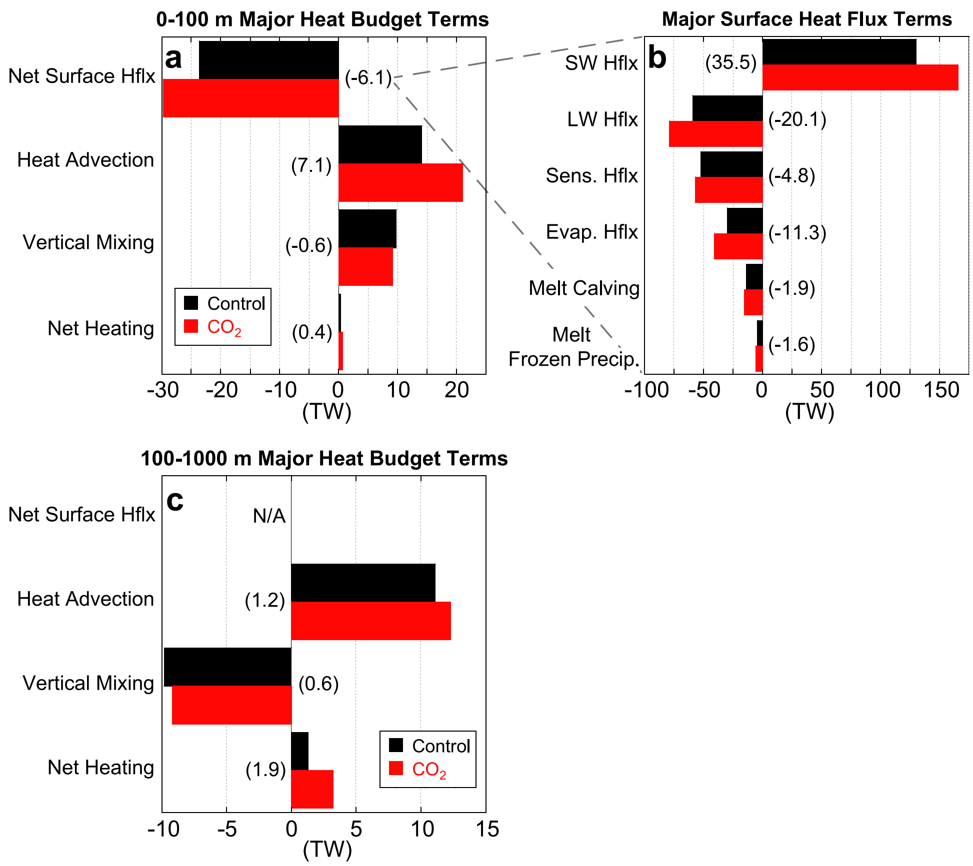

Figure 3. Major heat budget terms integrated over the (a, b) 0–100 m and (c) 100–1,000 m depth range for the Antarctic shelf region (TW). Years 62–80 averages of CM2.6 control (black), CO_2-forced (red), and CO_2-forced minus control (numbers in parentheses). Positive values reflect heat moving into the shelf region. The net surface heat flux is further divided into its major contributors (Figure 3b). Heat advection refers to the three-dimensional convergence of heat by resolved advection. Vertical mixing is the heat convergence due to vertical diffusion and the nonlocal tendency related to the KPP boundary layer parameterization (see section 3.3.2).

3.2.2. The 0–100 m Antarctic Shelf Region Advective Heat Transport

The convergence of the three-dimensional ocean advective heat flux at 0–100 m increases by 7.1 TW (or by 50%) in CM2.6 during years 62–80 of the 2xCO_2 experiment compared with the control simulation (Figure 3a). This advective heating works to offset the extra surface heat loss. To assess this increase in heat convergence, we calculate the cross-ASF lateral and vertical heat transport referenced to the minimum freezing point (see section 2.3).

In the control simulation, cross-ASF total volume and heat transport at 0–100 m is shoreward, largely due to the annual mean coastal Easterly wind stress (south of ~65°S, Figure 4) and resultant shoreward Ekman transport. Note, the control simulated zonal mean Easterly wind stress is strong relative to the time averaged (1981–2010) NCEP/NCAR and ERA-Interim reanalyses (Figure 4c; Dee et al., 2011; Kalnay et al., 1996). With CO_2 forcing, however, the CM2.6 zonal mean Easterly wind stress is more similar to the reanalyses.

In the control simulation, the cross-ASF shoreward volume transport is 6.1 Sv, which is primarily driven by the time mean component (supporting information Figure S8). In response to the CO_2 forcing, the peak Westerly wind stress shifts southward (by ~1° latitude) and the subpolar low deepens (by ~1–3 hPa) causing the coastal Easterly wind stress to weaken (Figures 4b–4d). The weakening leads to a small reduction of the cross-ASF total onshore volume transport for 0–100 m. Meanwhile, the ocean temperature increases in

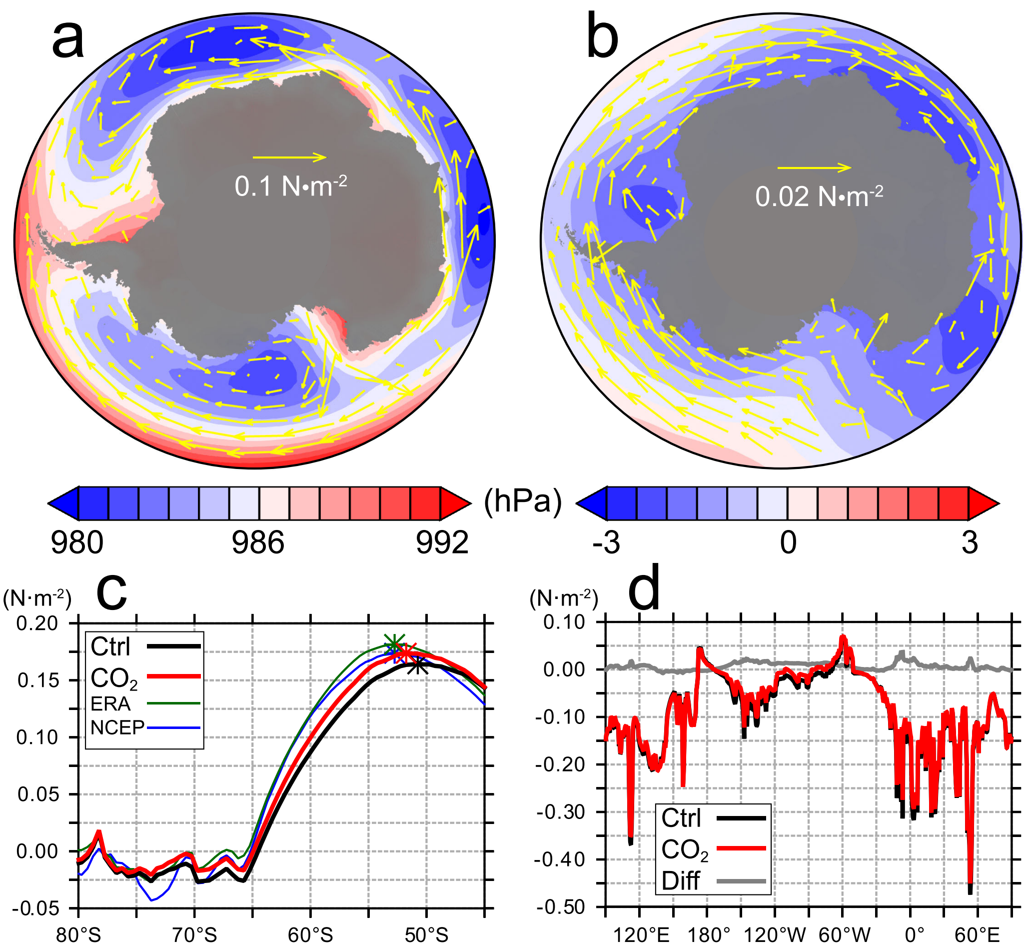

Figure 4. Years 62–80 average sea level pressure (slp, hPa) and surface wind stress to the ocean (N m^{-2}). (a) Control slp with wind stress vectors. (b) CO_2-forced minus control slp with wind stress anomaly vectors. (c) Zonal mean wind stress over the ocean, asterisk denotes location of maximum Westerly wind stress. Average of years 1981–2010 are used for the ERA-Interim (https://www.ecmwf.int/en/research/climate-reanalysis/era-interim) and NCEP/NCAR reanalyses (https://www.esrl.noaa.gov/psd/data/gridded/data.ncep.reanalysis.derived.surfaceflux.html). (d) Along-ASF wind stress. Negative values for the control and CO_2 experiment refer to Easterly wind stress. Positive values for the CO_2-forced minus control (gray) entail a weakening of the Easterly wind stress.

the 0–100 m layer under CO_2 forcing (Figure 2 and supporting information Figure S5). Despite the decreased shoreward volume transport in the upper 100 m, the near-surface warming causes shoreward heat transport to increase by 10.4 TW or by 27% (Figures 5a and 5e). This onshore total heat transport anomaly is driven by the time mean component and contributes to near-surface warming in the Antarctic shelf region.

Vertical advective heat divergence in the upper 100 m represents a downward movement of heat through the 100 m layer (Figures 6 and 7a). With CO_2 forcing, this vertical divergence increases by 3.8 TW or by 16%. In sum, the magnitude of the cross-ASF heat transport a nomaly is larger than the downward vertical heat transport anomaly, resulting in a net advective heat convergence in the top 100 m of 6.6 TW (an increase of 44%).

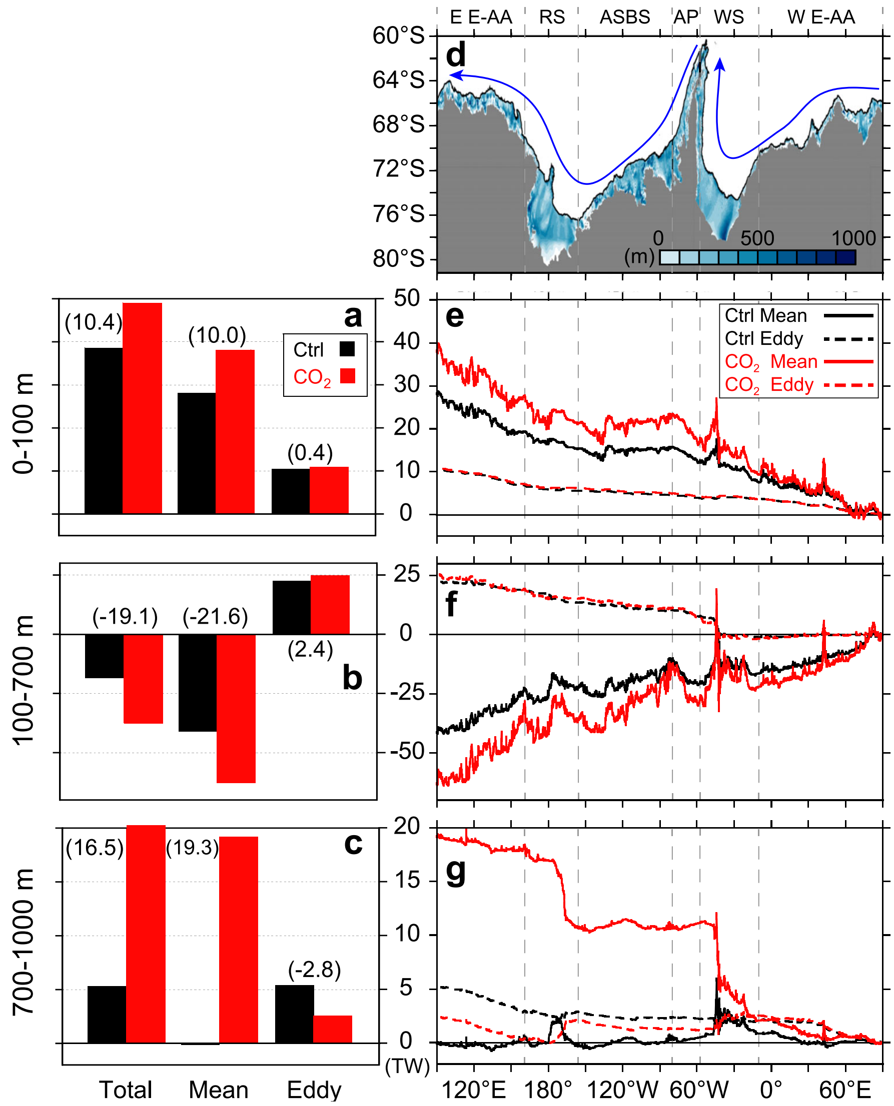

Figure 5. Years 62–80 average cross-ASF advective heat transport for three depth ranges for the Antarctic shelf region in the control simulation (black) and CO_2-forced (red, TW). (a–c) They chart the sum of transports for the three components and three depth ranges. Listed are the values of the CO_2-forced minus control simulation. (d) Shelf bathymetry from 0 to 1,000 m and the general route of the westward coastal current (blue arrows). (e–g) They graph the cumulative sum of transports from 90°E westward (to agree with the direction of the coastal current). The heat transports are referenced to the minimum freezing temperature and decomposed into the time mean and eddy components (see section 2.3). Positive (negative) transports are onshore (offshore) across the ASF "wall." Gray dotted lines through the right column figures mark the boundaries of the subdomains.

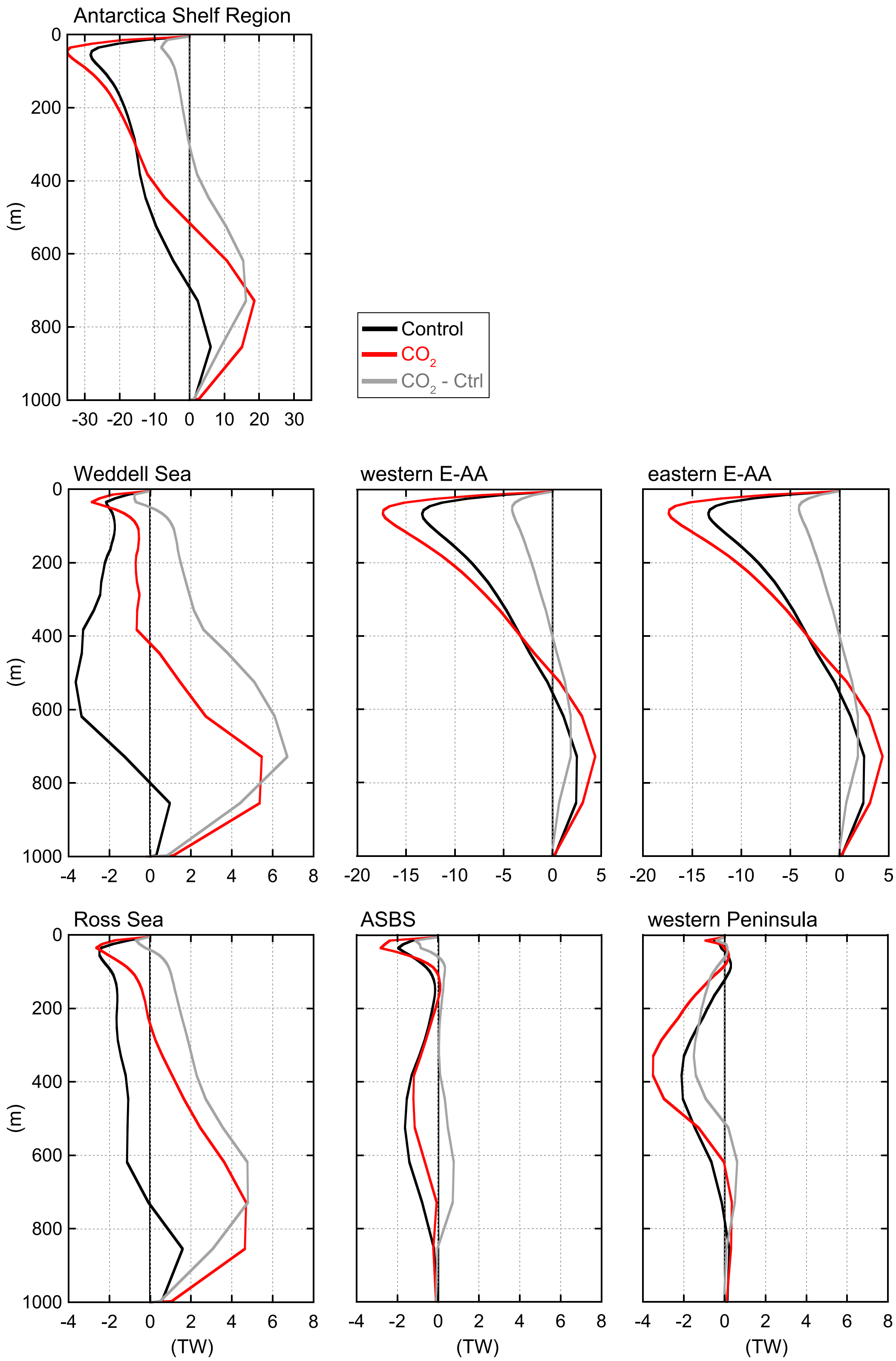

Figure 6. Depth profiles of years 62–80 average vertical advective heat convergence at each model depth layer (TW). For the control (black) and CO_2-forced (red) results, positive (negative) values indicate a convergence (divergence) of vertical transport at that depth level (closed circles mark the midpoint of a depth level). Note, divergence near the surface represents the downward transport of heat from the surface and divergence near 1,000 m represents upward transport of heat associated with CDW. In general, these transports cause convergence in the intermediate depths. The *x* axes range differs for each row.

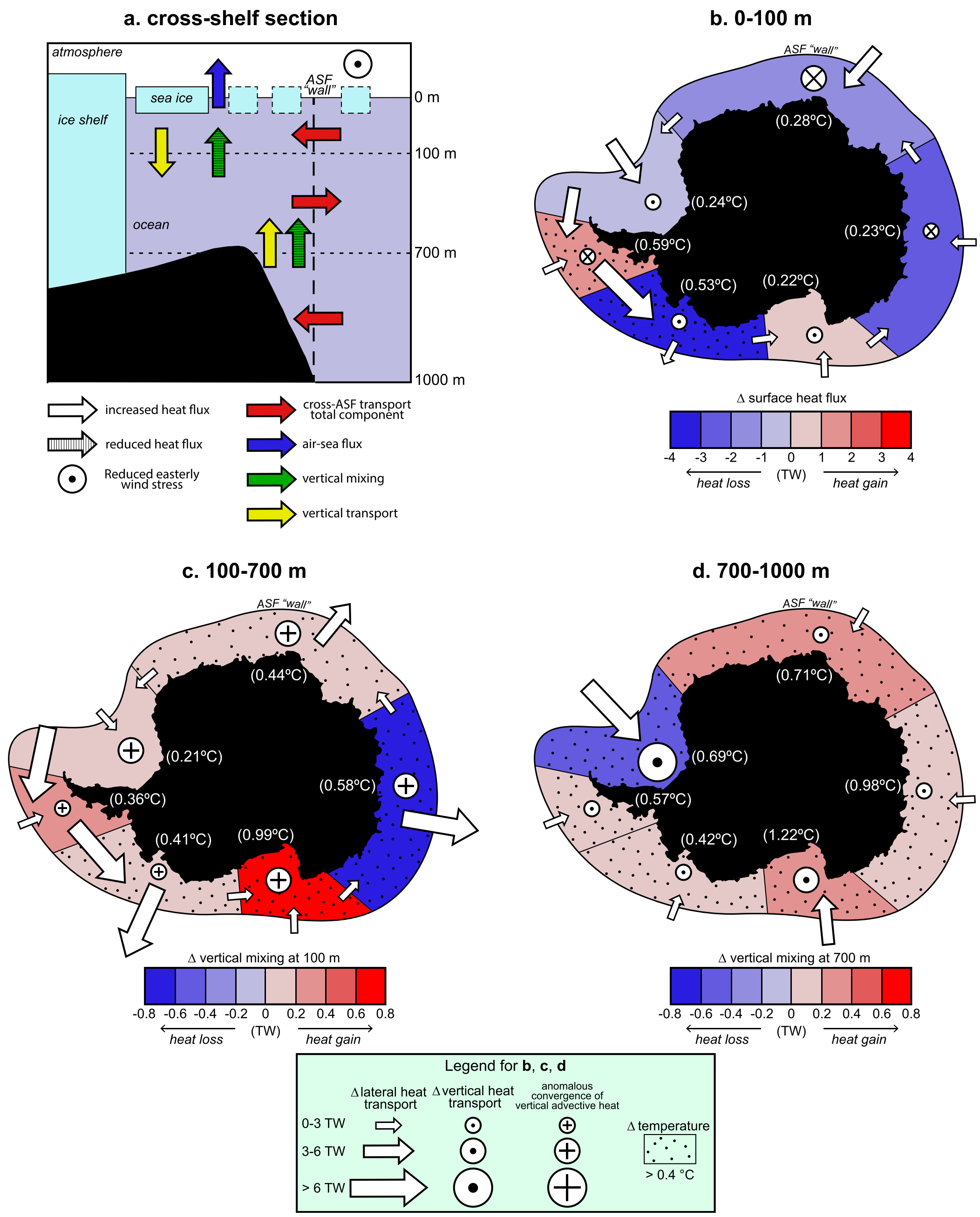

Figure 7. Schematic of the heat budget and temperature anomalies for the Antarctic shelf region and subdomains for the depth ranges of interest (TW, °C). (a) A generalized cross-shelf section showing the movement of heat anomalies for the Antarctic shelf region (note, the 0–100 m depth range is exaggerated to better show details). (b) For 0–100 m, cross-ASF and cross-subdomain boundaries heat transport anomalies (arrows), vertical advective heat transports through the 100 m layer (vertical arrows), surface heat flux anomalies (shading), and mean temperature change (stippling for >0.4°C and the text lists the numerical temperature change). (c) For 100–700 m, symbol references are similar to (Figure 7b) except the plus signs refer to vertical advective heat convergence and the shading refers to changes to the upward vertical mixing through the 100 m layer. (d) For 700–1,000 m, symbol references are similar to (Figure 7b) except vertical arrows refer to vertical advective heat transports through the 700 m layer and shading refers changes to the upward vertical mixing through the 700 m layer. Note, the cross-subdomain boundary heat transport anomalies are negligible at 700–1,000 m and are not included in the schematic.

3.2.3. The 0–100 m Spatial Variation of Shelf Region Warming

Figure 3a shows the increase in convergence of ocean heat advection for the upper 100 m (7.1 TW, note the heat transport values in the previous section are referenced to the freezing point and thus will not agree with this number, see section 2.3). This increase is partially compensated by a net cooling by the surface boundary fluxes (–6.1 TW) and reduced upward vertical heat mixing through the 100 m layer from below (–0.6 TW, the details of the vertical mixing of heat are discussed in section 3.3.2). Thus, a net heating of +0.4 TW remains and leads to 0–100 m warm anomalies across the Antarctic shelf region.

CM2.6 simulates a strong, narrow, predominately zonal and westward current around the entire Antarctic shelf break (supporting information Figure S9). This circumpolar current, as well as the ASF, differs from observations near the western Antarctic Peninsula and into the ASBS region. Here observations show a weaker ASF and more eastward/northward flow influenced by the nearby Antarctic Circumpolar Current and surface Westerly wind stress (Jacobs, 1991; Whitworth et al., 1998). As noted in section 2.1, the simulated ASF strength may be influenced by the incomplete resolution of mesoscale eddies at these latitudes which leads to reduced eddy induced transport and larger horizontal density gradients in the pycnocline. Nevertheless, the westward currents along the shelf break and above the shelf drive heat exchange through the lateral boundaries of the six subdomains (Figure 7b).

The lateral heat transports between subdomains are significant, with their magnitude equivalent to advective heat transports across the ASF "wall" and through vertical advection. Furthermore, the lateral heat transports between subdomains increase in the 2xCO_2 experiment (Figure 7b). This increase is due to both increased ocean heat content and volume transport of the westward shelf and shelf break currents. The ocean freshening on the shelf enhances the dynamic sea level gradient across the shelf break (Figure 1c). Thus, the geostrophic component of the shelf break current accelerates, which increases westward volume transport (supporting information Figure S9). This strengthening of the current offsets any weakening of the coastal current due to decreased Easterly wind stress (Figure 4).

In response to CO_2 forcing, the largest 0–100 m cross-ASF heat transport increase occurs in the Weddell Sea (Figure 7b). However, this subdomain does not simulate the largest warming. Instead, most of this heat is moved across the boundary between the Weddell Sea and the western Peninsula subdomain. This large upstream lateral boundary heat exchange and net downward surface boundary heat flux anomaly drives the relatively large warming of the western Peninsula surface ocean (0.59°C, Figures 2 and 7b). Despite the large warming, there is excess heat which moves downstream into the ASBS subdomain. This exchange contributes to the relatively large temperature anomaly at 0–100 m in the ASBS subdomain (0.53°C, Figure 2). This ASBS heating from the western Peninsula is partially compensated by an offshore cross-ASF heat transport anomaly (Figure 7b). Note, vertical advection and vertical mixing of heat play a secondary role in the western Peninsula and ASBS 0–100 m heat budget.

The four remaining subdomains simulate a more modest 0–100 m warming due to a more balanced heat budget (~0.25°C, Figure 2). In general, these four subdomains simulate increased cross-ASF heat transport and heat transport from the upstream subdomain (Figure 7b). This relative heating is compensated by more heat loss to the atmosphere, less upward mixing of heat from below the 100 m layer, and more heat loss through the downstream subdomain boundary. The one significant exception to this generalization occurs in the western East Antarctica subdomain. There, a relatively large onshore cross-ASF heat is compensated by increased divergence of vertical heat advection which moves the excess heat downward through the 100 m depth level (Figures 6 and 7b).

3.3. The 100–1,000 m Warming and Heat Budget

For the 100–1,000 m depth range, the volume-averaged Antarctic shelf region temperature increases by 0.59°C. The Ross Sea shows the largest warming (1.07°C, Figure 2). Except for the eastern East Antarctica subdomain, which warms by 0.71°C, the Ross Sea warming is more than double that of any of the other subdomains. From 100 to 1,000 m, the heat budget consists of lateral and vertical heat advection and the vertical mixing of heat. However, the heat budget is not balanced at these depths and leads to a local heating anomaly of +1.9 TW (or by 140%), driving the deep temperatures anomalies (Figure 3c).

3.3.1. The 100–1,000 m Antarctic Shelf Region Advective Heat Transport

With CO_2 forcing, the total three-dimensional convergence of ocean heat advection at 100–1,000 m increases by 1.2 TW (or by 10%, Figure 3c). To assess this increase in the Antarctic shelf region heat convergence, we calculate the cross-ASF and vertical heat transport referenced to the minimum freezing point (see section 2.3). Additionally, we make the calculations for both the 100–700 and 700–1,000 m ranges because the cross-ASF total heat transport reverses from offshore to onshore at ~700 m (Figures 5b and

5c), and, the vertical heat transport changes from divergent at deep depths to convergent at intermediate depths (Figure 6).

The cross-ASF eddy heat transport component and mean heat transport component work in opposite directions at 100–700 m, unlike the 0–100 m layer wherein both the time mean and eddy components are both onshore (Figures 5b and 5f). For the control simulation, the onshore eddy heat transport is 22.5 TW which is countered by an offshore mean heat transport of 41.0 TW. With CO_2 forcing, the onshore eddy heat transport moderately increases by 2.4 TW (or by 11%). However, the 100–700 m offshore mean heat transport increases more significantly by 21.6 TW (or by 50%), resulting in a total offshore heat transport through the ASF from 100 to 700 m (Figures 5b and 7a).

In the control simulation at 700–1,000 m, CM2.6 simulates a total onshore heat advection of 5.3 TW which is primarily a result of the eddy component (Figures 5c and 5g). However, under CO_2 forcing the mean flow becomes dominant. The mean component increases by 19.3 TW from $\sim$0 TW whereas the eddy component decreases by 2.8 TW (or by 50%). The switch of the dominant onshore transport from eddy to mean flow at 700–1,000 m in the 2xCO_2 experiment is discussed in section 4.1. In sum, under CO_2 forcing, the 700–1,000 m total onshore heat transport increases by 16.5 TW (or by 300%), primarily due to its time mean component (Figures 5c and 5g).

Vertical advective heat transport in the Antarctic shelf region works to disperse the onshore cross-ASF heat anomalies at 700–1,000 m into the above water. This upward heat flux initiates vertical advective heat divergence at 700–1,000 m and convergence of vertical advective heat at 100–700 m (Figure 6). With the addition of downward heat advection from 0 to 100 m, the redistribution of heat in the vertical works to spread positive temperature anomalies near the surface and at deep depths to the intermediate depths (Figure 2). Furthermore, as a response to the vertical heat convergence at 100–700 m, some of the excess heat at the intermediate depths is transported laterally offshore through the ASF (Figure 7a).

3.3.2. The 100–1,000 m Antarctic Shelf Region Vertical Mixing of Heat

Previous studies show surface freshening in the Southern Ocean can lead to reduced vertical mixing of heat by gravitational instability between the surface and warmer waters below. For example, reduced vertical mixing of heat can result in sea ice expansion (Bintanja et al., 2013), slow abyssal overturning (Morrison et al., 2015), or both (Aiken & England, 2008). Here we focus on freshwater forcing and the response of vertical mixing of heat on the continental shelf rather than in the broader domain of the Southern Ocean and large-scale overturning circulation. We hypothesize that surface freshening can restrict upward mixing of heat, thus confining warm waters to the deep layers. To evaluate this hypothesis, we look for a covarying relationship between the Antarctic shelf region warming at depth and the surface freshening, and examine the response of mixing of heat to CO_2 forcing.

Correlations between the time series of the 0–100 m salinity anomalies and the 100–1,000 m temperature anomalies for each subdomain show the shallow freshening anomalies precede the deeper warm temperature anomalies by 1–3 years (Figure 8, line graphs). The correlation of the detrended time series is significant, $\sim$0.70 for the Weddell Sea, eastern and western East Antarctica, and the Ross Sea. The correlation is lower ($\sim$0.35) for the ASBS and western Peninsula subdomains, yet is still significant at 99% confidence. Salinity and temperature anomalies covary with time as well as by the magnitude of the anomalies (Figure 8, shaded plots). Next, we investigate the mechanism for this correlation by looking at vertical mixing of heat.

Vertical mixing in CM2.6 occurs at the subgrid scale and is thus parameterized. We define vertical mixing as the sum of vertical diffusion and the nonlocal tendency related to the KPP boundary layer parameterization (Large et al., 1994). The KPP parameterization includes a nonlocal transport that aims to account for such processes as boundary layer eddies whose transport may be unrelated to the local vertical gradient of the mean field. Vertical mixing is sensitive to changes in the vertical temperature gradient and vertical diffusivity (which is sensitive to salinity forcing), as well as buoyancy and mechanical forcing at the surface. Figure 9 shows the depth profile of cumulative sum of the vertical mixing for each Antarctic shelf region subdomain, summed from the bottom upward. A positive (negative) value entails upward (downward) transport of heat.

Given the vertical mixing parameterization, the CO_2-forced shelf freshening reduces vertical diffusivity (supporting information Figure S10) and increases vertical stratification. As a result, upward mixing of heat decreases especially between 100 and 200 m. Indeed, a reduced vertical mixing anomaly near $\sim$100 m

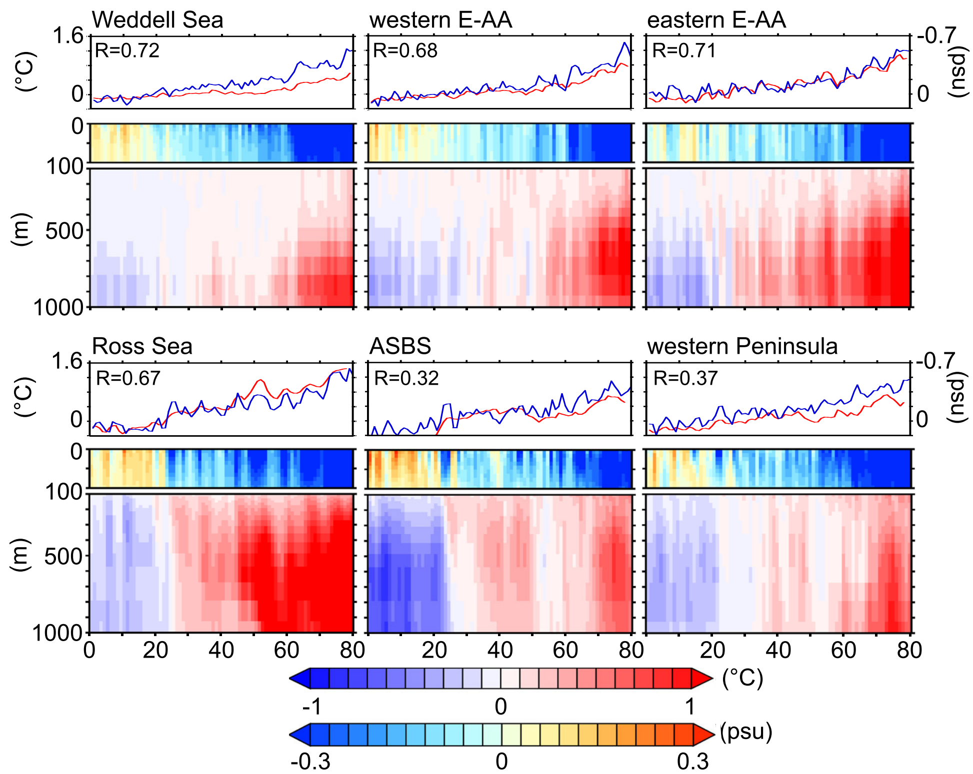

Figure 8. Temporal correlation between the 0–100 m salinity anomalies (freshening is blue, psu) and the 100–1,000 m temperature anomalies (°C). The anomalies are calculated as the difference between each of the 80 years of the CO_2-forced simulation and the years 62–80 control average. For each subdomain, the top figure is the time series of the 0–100 m salinity anomalies (blue line, right *y* axis; note inverted scale) and the 100–1,000 m temperature anomalies (red line, left *y* axis). Listed is the detrended correlation between the two time series, with the best correlation occurring when the temperature anomaly lags the salinity anomaly by 1–3 years (temperature anomaly time series are shifted according to lag). All correlations are significant at 99% confidence. The middle and bottom figures show the 0–100 m salinity anomalies versus depth and time and the 100–1,000 m temperature anomalies versus depth and time, respectively.

occurs in all subdomains except in eastern East Antarctica (Figures 7c and 9), resulting in a total reduction of upward heat mixing through the 100 m level for the Antarctic shelf region at 0.6 TW (or by 6%, Figure 3c). This 0.6 TW reduction of upward heat mixing explains 32% of the net heating anomaly from 100 to 1,000 m (Figure 3c). These results suggest that the CO_2-induced freshening reduces the upward mixing of excess shelf heat and contributes to warm temperature anomalies at 100–1,000 m.

Negative anomalies of the vertical mixing of heat are also present at greater depths, which are distinguishable from the anomalies near 100 m (Figure 9). As indicated by the difference between the control and CO_2 runs, the freshening anomalies (Figure 10, see contours) fill the shelf and alter the isopycnals (Figure 11, see contours), often down to the depth of the shelf break. These freshening anomalies reduce diffusivity and vertical mixing even at deep depths (700–1,000 m). This reduction of vertical mixing limits upward movement of heat at the same depth where there is increased cross-ASF onshore heat transport (Figures 5c, 7a, and 9). The combination of reduced upward mixing of heat and increased cross-ASF onshore heat transport hastens the buildup of positive heat anomalies at 700–1,000 m depths. As these heat anomalies build, they can only be dispersed from 700 to 1,000 m by vertical heat advection, as lateral heat transport between subdomains at these depths are negligible (Figures 7a and 7d).

3.3.3. The 100–1,000 m Spatial Variation of Shelf Region Warming

The 100–1,000 m increase in heat convergence by the three-dimensional advective field (1.2 TW) and by reduced upward mixing of heat (0.6 TW), results in a net heating of 1.9 TW and an Antarctic shelf region warming of 0.59°C at these depths (Figure 3c). The subdomain temperature anomalies at these depths are controlled by these two processes, as well as lateral heat transports across the subdomain boundaries. Here we present important features of each subdomain's heat budget and introduce another mechanism in which shelf freshening controls shelf warming.

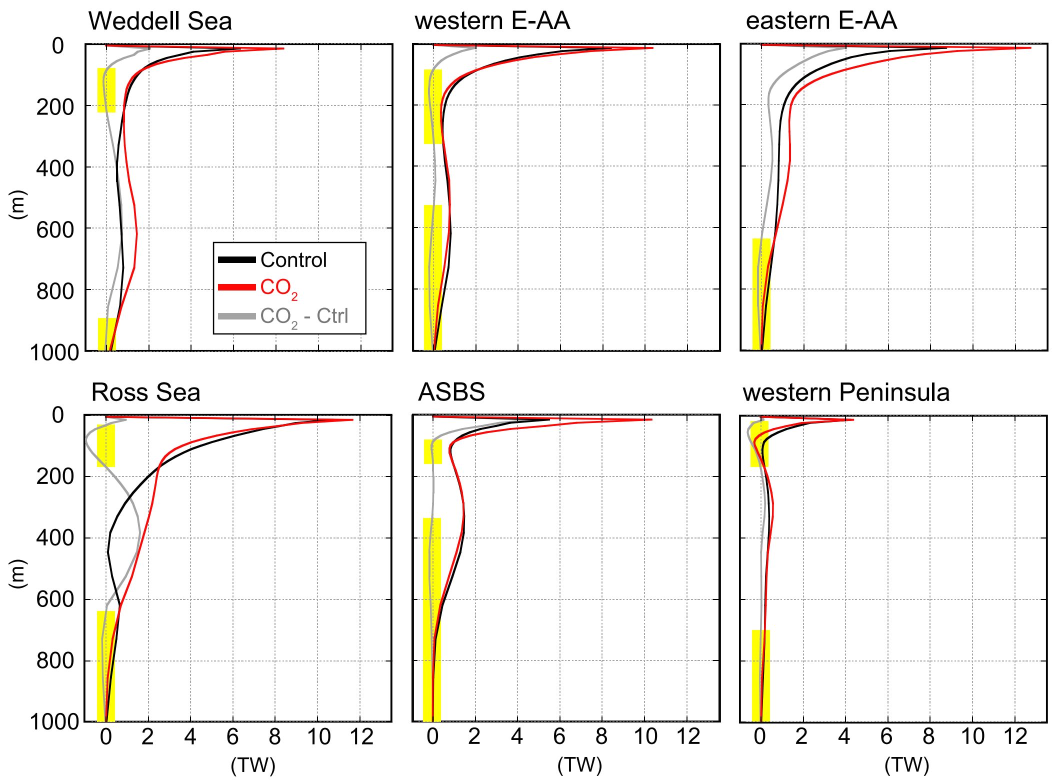

Figure 9. Depth profiles of vertical mixing of heat (sum of vertical diffusion and the nonlocal tendency related to the KPP boundary layer parameterization) for each subdomain (TW). Results are from the control simulation (black), CO_2-forced (red), and CO_2-forced minus control (blue) averaged from years 62 to 80. These profiles result from cumulatively summing the heat mixing tendencies from 1,000 m to the surface. A positive value corresponds to a net upward transport of heat for a given depth, as referenced to a zero transport at the ocean bottom. Yellow highlights denote depths where the vertical heat transport is smaller in the CO_2-forced simulation than the control.

The Weddell Sea shows an onshore cross-ASF heat transport anomaly at 700–1,000 m (Figures 5g and 7d). The onshore cross-ASF heat transport anomaly is driven by a large CO_2-forced time mean component at 700–1,000 m depths located between ~20°W and 45°W in the Weddell Sea subdomain (Figure 5g). Unlike the control, the CO_2-forced onshore spike is not compensated by an offshore heat transport just west of ~45°W; rather, the heat remains onshore of the ASF "wall." Yet, the heat does not penetrate coastward onto the shelf nor significantly warm the waters above the shelf floor (Figures 1a and 11). Instead, the heat anomalies and subsequent warming shoreward of the ASF "wall" are restricted to the shelf slope. We find shelf freshening to be the cause of this restriction.

Unlike the large fresh anomalies in the other subdomains, the comparatively large anomalies (greater than 0.20 psu) are found along the full length of the ASF in the Weddell Sea subdomain and reach the shelf slope (Figures 1b and 10 and supporting information Figure S5). As a response to the freshening, the lateral density gradient increases and the isopycnals steepen at the ASF and at the Weddell Sea shelf slope (Figures 10 and 11). At depths 700–1,000 m, this response disconnects isopycnals between the Weddell Sea shelf and CDW making it difficult for heat to reach the shelf floor and spread across the subdomain. In turn, the 700–1,000 m cross-ASF onshore heat transport anomaly and subsequent warming is confined to the region between the shelf break and ASF "wall" (Figure 11). Unable to penetrate coastward, much of this heat is advected upward before moving downstream at intermediate depths to the western Peninsula subdomain (Figures 6 and 7c and 7d). Note, the heat transports across lateral boundaries at 700–1,000 m are negligible, therefore, the heat does not move downstream until reaching intermediate depths.

In contrast to the widespread and deep freshening anomalies in the Weddell Sea subdomain, the other subdomains include locations where the 0–100 m freshening anomaly near the shelf break and ASF "wall" is less pronounced (less than 0.20 psu, supporting information Figure S5). At these locations, the freshening

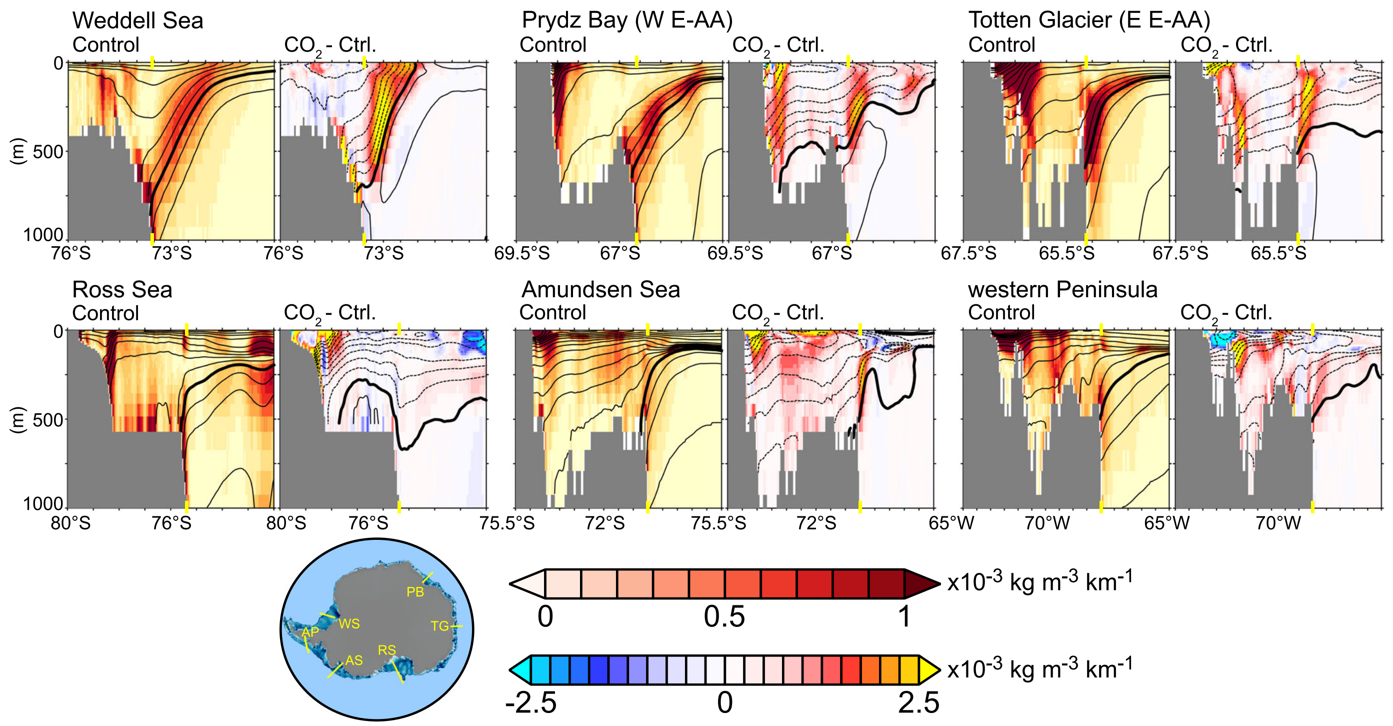

Figure 10. Cross-shelf transects of the lateral potential density (referenced to the surface) gradient ($\times 10^{-3}$ kg m^{-3} km^{-1}, shaded) with contours of constant salinity (psu, black lines) for locations in each of the subdomains for years 62–80. The control figures have 0.1 psu contour levels with the 34.4 psu contour level in thick black. The CO_2-forced minus control figures have 0.05 psu contour levels. Dotted lines entail a reduction of salinity and the solid thick line is the 0 psu contour, where no salinity change occurs. The small yellow ticks on the *x* axes mark the top and bottom of the ASF "wall." The transect locations are the same as in Figures 11 and 12. Note, the Prydz Bay cross-shelf profile is located in the western East Antarctica region and the cross-shelf profile near the Totten Glacier is located in the eastern East Antarctica region. The map insert shows the exact location and length of each transect plotted over shelf bathymetry.

effect on the cross-ASF density gradient and steepening of the isopycnals near the shelf break is less abrupt than what occurs in the Weddell Sea subdomain (Figures 1d, 10, and 11). We select five locations, one for each of the other subdomains, to compare with the Weddell Sea location. At these locations, weaker freshening anomalies at 0–100 m lead to weaker anomalies the shelf break and ASF "wall" (Figure 10 and supporting information Figure S5).

We note that the years 62–80 mean freshening anomalies at ~200–1,000 m (Figure 10 and supporting information Figure S5), result from both descending freshening anomalies from the surface and, the positive salinity anomalies associated with relatively salty CDW reaching the shelf during these years. Therefore, the spatial coherence between freshening anomalies and warm anomalies in Figures 1a and 1b (particularly at 200–1,000 m depth, supporting information Figure S5), is largely driven by CDW intrusions, which reduce the local freshening. However, time series, rather than the time mean anomalies, show 0–100 m salinity anomalies lead 100–1,000 m temperature anomalies, suggesting freshwater may reach the shelf break and strengthen the lateral density gradient of the ASF before CDW intrusions occur (Figure 8). Conversely, where 0–100 m salinity anomalies are weak near the shelf break (e.g., Ross Sea, supporting information Figure S5), the ASF does not strengthen as much and results in the region being more susceptible to CDW intrusions and positive temperature anomalies at depth. Our ongoing work, regarding the Antarctic shelf region freshwater budget and the timing of freshwater anomalies at the shelf break, will lead to increased understanding of freshening effects on cross-ASF heat transport.

The Ross Sea offers a good example of cross-ASF heat transport penetrating the shelf and driving large temperature anomalies at depth. From 100 to 1,000 m, the Ross Sea warms by 1.07°C (Figures 1a and 2). This anomaly is primarily driven by increased 700–1,000 m onshore cross-ASF mean heat transport and a reduction of upward vertical mixing of heat at depth (Figure 7d). Similar to the Weddell Sea subdomain, CO_2-forced onshore cross-ASF mean transport from 700 to 1,000 m also spikes in the Ross Sea subdomain

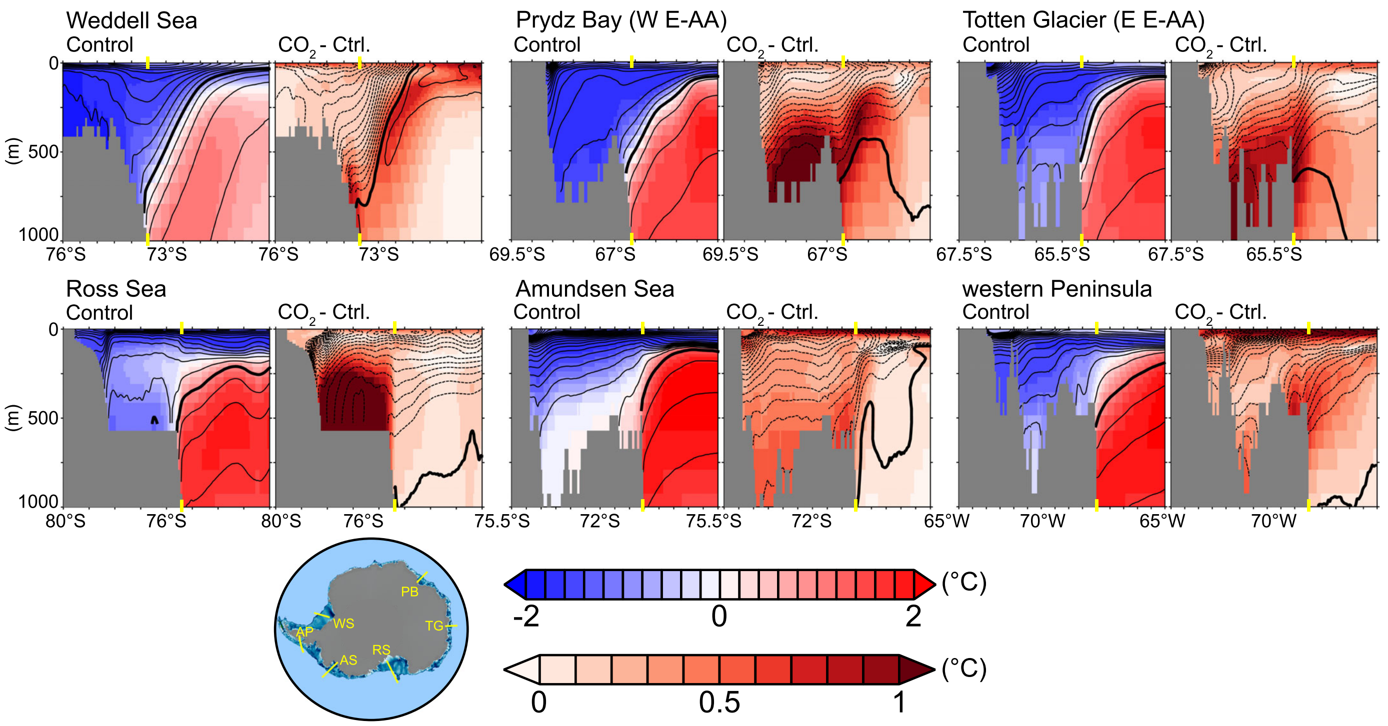

Figure 11. Cross-shelf transects of potential temperature (°C, shaded) with isopycnal contours of potential density referenced to the surface (kg m^{-3}, black lines) for locations in each of the subdomains for years 62–80. The control figures have 0.5 kg m^{-3} isopycnal contour levels with the 27.6 kg m^{-3} contour level in thick black. The CO_2-forced minus control figures have 0.2 kg m^{-3} isopycnal contour levels. Dotted lines entail a reduction of potential density and the solid thick line is the 0 kg m^{-3} contour, where no density change occurs. The small yellow ticks on the x-axes marks the top and bottom of the ASF "wall." The transect locations are the same as in Figures 10 and 12.

(Figure 5g, between ~165°W and 178°W). Without an offshore transport to west of ~178°W to balance the onshore transport (as in the control simulation), this heat anomaly remains shoreward of the ASF "wall."

The Ross Sea subdomain freshening near the shelf break and corresponding lateral density gradient increase at the ASF "wall" is much weaker compared to that of the Weddell Sea subdomain (Figures 1b and 1d). Therefore, the isopycnal structure is less restrictive of heat associated with CDW crossing into the subdomain (Figure 11). Once on the shelf floor, the heat is advected laterally and vertically, warming most of the subdomain (Figures 1a, 6, and 11). Additionally, heat further accumulates at depths greater than 100 m because the vertical mixing of heat decreases at depths ~625 to 1,000 m and again at the 100 m layer (Figure 9). As a consequence, upward mixing of heat slows and less heat at depth is moved into the surface layer by this mechanism. Hence, without a large downstream heat transport anomaly to the eastern East Antarctica subdomain (Figures 7c and 7d) or a cross-ASF offshore heat transport anomaly at 100–700 m (Figure 7c), the Ross Sea subdomain experiences a large convergence of heat and warming from 100 to 1,000 m.

From 100 to 1,000 m, the eastern and western East Antarctica subdomains warm by 0.71°C and 0.53°C, respectively. Here we focus on a location near the Totten Glacier (eastern East Antarctica) and a location within the Prydz Bay (western East Antarctica). Both locations warm by ~1°C above the shelf floor (Figure 11). This warming from 700 to 1,000 m benefits from a deep shelf break and shelf floor. At these depths, cross-ASF onshore heat transport can occur below the depth of the large freshening anomalies and large increases in the ASF lateral density gradient without being blocked or constrained by the continental slope (Figures 10 and 11). Over time, heat flows across the shelf floor and its movement upward is influenced by vertical mixing and vertical advective transport. Upward vertical mixing below ~600 m is slowed in both subdomains by the local freshening, helping to build up heat and temperature anomalies at depth (Figure 9). Meanwhile, the upward vertical advective transport moves heat to intermediate depths, helping to disperse the heat and warm the waters above (Figures 2 and 6). At 100–700 m, some of the heat is moved downstream to other subdomains or is transported offshore through the ASF (Figure 7c).

The chosen locations in the western Peninsula and ASBS also show increased warming at depth (Figure 11). Similar to the eastern and western East Antarctica subdomains, the relatively deep shelf break and shelf floor allows cross-ASF onshore heat transport to occur below the depth of the large freshening anomalies and strong lateral density gradients (Figure 10). However, the correlation between surface freshening and deep shelf warming is about 50% less for the western Peninsula and ASBS when compared to the other subdomains (Figure 8). We attribute the weaker correlation to the influence of large lateral heat transport anomalies, which mask the surface freshening and deep warming relationship. The western Peninsula subdomain is supplied with relatively large heat transports from the Weddell Sea subdomain from the surface to 700 m and transports much heat downstream to the ASBS subdomain (Figures 7b and 7c). Besides receiving a large heat anomaly from the western Peninsula, ASBS also transports much heat offshore through the ASF at 100–700 m. These large lateral fluxes control much of the heat budget, so the relationship between freshening and deep warming is somewhat muddled in the western Peninsula and ASBS subdomains. Nonetheless, the surface freshening does reduce vertical mixing of heat below 100 m and works to accumulate heat anomalies at depth (Figures 2 and 9). The overall 100–1,000 m warming response is 0.44°C and 0.42°C for the western Peninsula and ASBS subdomain, respectively.

4. Discussion

4.1. Role of Freshening in the Warming of the Antarctic Shelf Region

CO_2 forcing significantly warms and freshens the Antarctic shelf region. We find the surface freshening can work to both prevent and enhance heat convergence at depth, making shelf freshening a possible control of the location, magnitude, and timing of deep shelf warming (Figures 1a and 1b and 8 and supporting information Figure S5). Shelf freshening slows upward vertical mixing at depth, acting as a freshwater-cap to build positive temperature anomalies at depth. By contrast, shelf freshening also works to strengthen the lateral density gradient and steepen the isopycnals associated with the ASF. This process limits cross-ASF connecting isopycnals and cross-ASF heat transport (Isachsen, 2011; Stewart & Thompson, 2015). Therefore, along the ASF where surface freshening anomalies are large and eventually reach depths below the shelf break, deep cross-ASF heat transport is prevented from entering the Antarctic shelf region or is confined to the small region between the ASF and the shelf slope at deep depths. We note that the freshening anomalies must develop before anomalous onshore heat transport begins to be most effective. A better understanding this temporal relationship at the ASF and its influence on the location of large temperature anomalies on the shelf is part of ongoing research.

Nonetheless, there are many locations along the ASF "wall" where increased 700–1,000 m onshore heat transport develops warm temperature anomalies above the shelf. However, the 700–1,000 m cross-ASF onshore heat transport anomaly is not driven by the eddy component as shown by previous studies (e.g., Hattermann et al., 2014; Nøst et al., 2011; Stewart & Thompson, 2015). Instead, we find that the time mean component brings excess heat across our defined ASF "wall." Below we discuss this inconsistency with earlier research and consider mechanisms that may initiate the onshore transport of heat and formation of warm anomalies at depth in CM2.6.

4.2. Limitations of CM2.6 Regarding Cross-ASF Eddy Heat Transport

One reason for the minor role played by eddies in the cross-ASF heat transport could be that the model resolution of CM2.6 is not fine enough to fully capture eddy heat transport near the ASF. Along the Antarctic shelf break, the model grid spacing ranges from 4 to 6 km. Previous studies show that refining the grid spacing at the shelf break from $>$2 km to $\sim$1 km increases cross-ASF eddy transport (Årthun et al., 2013; Stewart & Thompson, 2015). Additionally, an ocean grid resolution of $\sim$1 km better captures topographic waves and onshore eddy heat transport triggered by the interaction of the Antarctic shelf break current and troughs and canyons that cut into the shelf slope (e.g., Dinniman et al., 2011; Moffat et al., 2009; St-Laurent et al., 2013). Furthermore, the increased mesoscale eddy activity at a 1 km ocean grid spacing would increase lateral transport across the ASF and work to flatten the isopycnals locally. Such a flattening would generate more isopycnals with slopes parallel to the continental slope, promoting more cross-ASF eddy tracer transport and introducing new density classes with access to the shelf (Isachsen, 2011).

Another reason for the reduced eddy heat transport at 700–1,000 m in CM2.6 could be the absence of simulated dense shelf water overflows. For example, in the Weddell Sea these overflows of Antarctic Bottom

Water cascade down the continental slope and shoal nearby CDW (Orsi et al., 1999). The shoaling allows additional CDW density classes to have access to the continental shelf (Stewart & Thompson, 2016). However, in CM2.6, the Weddell Sea overflows do not reach depths greater than ~1,500 m (Dufour et al., 2017). Instead, the dense saline waters on the shelf tend to mix with waters across the ASF at intermediate depths and thus lose their water mass properties. This spurious diapycnal mixing is a well-known bias in level coordinate ocean models (e.g., Danabasoglu et al., 2010; Winton et al., 1998). For our study, the absence of Antarctic Bottom Water flowing along the shelf slope to the abyssal ocean eliminates a possible isopycnal pathway for eddy heat transport between the CDW and shelf (Stewart & Thompson, 2016).

An alternative explanation to the reduced eddy heat transport at 700–1,000 m may reside with our definition and location of the ASF "wall." The ASF "wall" is a vertical line from the surface to the 1,000 m isobath. As such, the ASF "wall" does not fully capture the simulated ASF, which slopes down from near the surface to the shelf break and whose position fluctuates with time (Figure 11, see contours in control figures). Consequently, the ASF "wall" at greater depths tends to reside at or below the boundary between the shelf waters and CDW. With CO_2 forcing, this boundary shoals, placing more of the ASF "wall" below the simulated ASF and well within the CDW (Figure 11 and supporting information Figure S11). Thus, the ASF "wall" is not recording the heat transport crossing the bottom of the simulated ASF as in the control simulation. Instead, the ASF "wall" is recording the time mean component of CDW heat moving shoreward before being transported through the missing segment of the simulated ASF.

Such a scenario causes the recorded onshore eddy heat transport to decrease and onshore mean heat transport to increase at 700–1,000 m (Figure 5c). Furthermore, the anomalous onshore heat transport of the time mean component at 700–1,000 m (19.3 TW, Figure 5c), provides an upper limit to the amount of heat passing through the simulated ASF near the shelf slope that is missed by our ASF "wall" definition. This heat transport through the simulated ASF likely has a large eddy component given that during the control simulation, wherein the ASF "wall" coincides better with the simulated ASF at 700–1,000 m, the onshore heat transport was exclusively by eddies (Figure 5c). Thus, our methods miss part of the 700–1,000 m onshore eddy heat transport through the simulated ASF.

4.3. Proposed Mechanisms for Increased Onshore Heat Transport

This study focuses on CO_2-forced changes to the Antarctic shelf region heat budget that lead to surface and deep warming on the shelf. Here we expand on a few mechanisms that may initiate the movement of CDW heat toward the shelves.

Of particular relevance to our results, Nøst et al. (2011) show shelf region freshening increases local buoyancy and available potential energy on the shelf. The available potential energy is released through increased eddy kinetic energy (EKE) which drives onshore cross-ASF eddy transport at depth. In CM2.6, the shelf freshening leads to an increase in the cross-shelf dynamic sea level gradient and a corresponding velocity increase of the westward coastal current (Figure 1c and supporting information Figure S9). As a response to the faster current, EKE also increases near the ASF and down to the depth of the shelf break (Figure 12). Accepting that our ASF "wall" misses part of the onshore eddy heat transport at 700–1,000 m in the 2xCO_2 experiment (see end of section 4.1), then it is possible that the increased EKE near the shelf break is driving more onshore eddy heat transport at 700–1,000 m. This EKE-driven increase in onshore eddy heat transport would agree with changes for both variables at 0–100 and 100–700 m (Figures 5e, 5f, and 12). However, despite increased EKE, the larger and deeper lateral density gradients from the freshening can prevent excess heat from reaching the shelf floor by restricting and disconnecting isopycnals between the shelf water and the CDW. Hence, there exists a balance between freshening increasing EKE near the ASF, and freshening increasing the isopycnal barrier to onshore eddy heat transport.

Next, we comment on two mechanisms that shoal isotherms near the shelf break and lead to increased transport of warm CDW onto the Antarctic shelf (Spence et al., 2014, 2017). First, Spence et al. (2014) find that weaker Easterly wind stress and related decrease of Ekman pumping shoals isotherms and isopycnals near the shelf break, introducing new pathways for CDW to reach the shelf. A similar process is found in the CM2.6 results. With CO_2 forcing, the peak Westerly wind stress strengthens and shifts poleward by about 1°, while the coastal Easterly wind stress (65°S–75°S) weakens (Figure 4). These wind changes as well as a low-pressure anomaly above the continent (Figure 4) agree with observations, reanalysis data, and climate

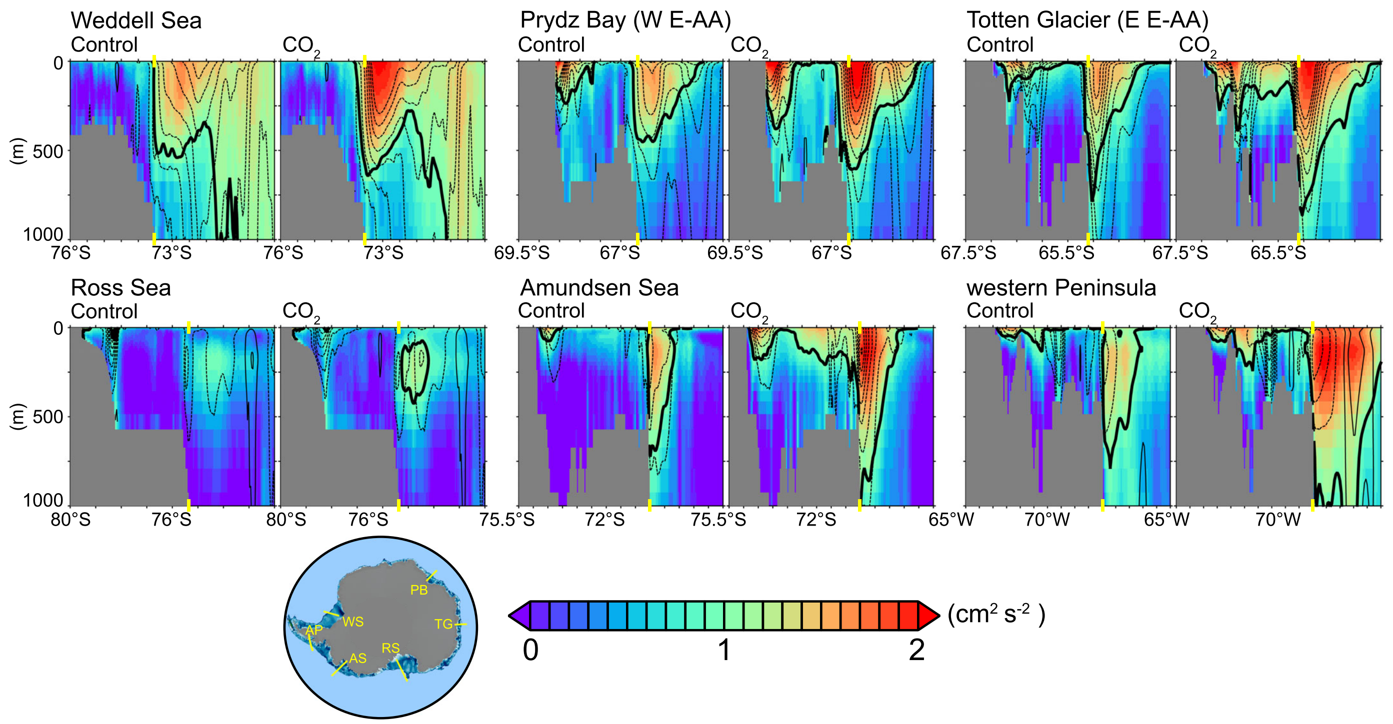

Figure 12. Cross-shelf depth transects of the logarithm of eddy kinetic energy (EKE, shaded and thick contour) and zonal current velocity (contours) for the control simulation and $2xCO_2$ experiment ($cm^2\ s^{-2}$, $cm\ s^{-1}$). EKE is calculated using every fifth day, daily mean fields of zonal and meridional current velocities during a three-year period from years 69 to 71, using methods based on Stevens and Killworth (1992). We add a the thick contour where EKE equals 1 $cm^2\ s^{-2}$ to assist with comparison between the two simulations. The thin contours are zonal current velocity with intervals of 2 $cm\ s^{-1}$. Dotted thin contours entail westward zonal flow. Note, the westward flow near the shelf break increases with CO_2 forcing as does EKE. The small yellow ticks on the *x* axes mark the top and bottom of the ASF "wall." The transect locations are the same as in Figures 10 and 11.

model data of a recent trend toward a positive Southern Annular Mode index (e.g., Marshall, 2003; Swart & Fyfe, 2012; Thompson & Solomon, 2002). The weakened Easterly wind stress reduces poleward Ekman transport and associated downwelling in the shelf region (supporting information Figure S12). Therefore, the shoaling of isotherms near the shelf break (Figure 11 and supporting information Figure S11) may be a response to reduced Easterly wind stress as found by Spence et al. (2014). However, shelf freshening in CM2.6 prevents the wind changes from shoaling the isopycnals at the ASF.

Second, Spence et al. (2017) identify a shelf wave mechanism that can shoal isotherms near the shelf break and lead to shelf warming. The isotherms shoal due to a compensation between barotropic pressure gradients and baroclinic adjustments through arrested bottom Ekman processes (e.g., MacCready & Rhines, 1993; Wåhlin et al., 2012). To shoal warm isotherms, the shelf wave mechanism requires an anomalous sea level low next to the coast. As their study shows, this low sea level can be induced by weakening Easterly wind stress. However, in our simulations, coastal freshening dominates wind-driven changes to the dynamic sea level. The large halosteric sea level rise leads to an anomalous positive dynamic sea level near the coast (Figure 1c). In turn, arrested Ekman layer dynamics will act to deepen isotherms rather than shoal them.

Thus, both Spence et al. (2014, 2017) demonstrate wind-driven mechanisms that shoal isotherms. In CM2.6, the wind trends are weaker than those found in either Spence et al. (2014) or Spence et al. (2017). Nonetheless, isotherms do shoal with CO_2 forcing (Figure 11 and supporting information Figure S11), which promotes cross-ASF onshore transport of lighter density classes (supporting information Figure S13). However, shelf freshening works against wind-forced isotherm shoaling by reversing the arrested Ekman layer dynamics and works against onshore heat transport by increasing the lateral density gradient at the ASF. These compensating effects from freshening is absent in Spence et al. (2014, 2017), possibly because precipitation and runoff were held constant in their experiments. Our results point to the importance of both freshening and wind changes in determining the ability of warm CDW to cross the ASF front.

5. Conclusions

Using a global coupled climate model with an active mesoscale eddying ocean component, we investigated the spatial and temporal characteristics of ocean warming and climate change near Antarctica caused by a 1% per year increase of the atmospheric CO_2 concentration. We find that different mechanisms cause significant ocean warming in the upper 100 m (0.33°C) as compared to the ocean warming at 100–1,000 m (0.63°C, Figure 7). The near-surface ocean warming is primarily a response to enhanced onshore advective heat transport across the shelf break. Some of this heat is counteracted by a larger ocean-to-air heat flux resulting from decreased sea ice coverage allowing for more interaction between the ocean and atmosphere. Furthermore, excess heat in the 0–100 m layer can be transported downstream (westward) to other areas of the shelf region, thereby contributing to local warming (Figure 7b).

Below 100 m, the deep ocean warming on the shelf is controlled by the cross-Antarctic Slope Front (ASF) transport of warm Circumpolar Deep Water (CDW) and by large freshening anomalies supplied at the surface and near the ASF. The deep temperature anomalies occur ~1–3 years after the local salinity anomalies suggesting a relationship between the two anomalies. The ocean freshening on the shelf limits vertical mixing of heat, notably at ~700–1,000 m depths where CDW enters the shelf region. This reduction in upward heat mixing partially prevents heat that is associated with CDW from moving toward the ocean's surface and out of the water column (Figures 7c and 7d). Thus, helping the formation of warm anomalies at depth. Additionally, freshening can increase and deepen the lateral density gradients associated with the ASF (Figures 1d and 10). Such enhancement of the ASF can work to prevent onshore heat transport associated with the CDW. Lastly, the freshening enhancement of the ASF also suppresses onshore heat transport associated with nearby increases in eddy kinetic energy and shoaling of isotherms (Figures 10–12). Therefore, CO_2-induced shelf freshening influences numerous heat transport mechanisms. Continued understanding of the interaction between freshening and these mechanisms will help inform future shelf warming at depth.

The near-surface and deep warming both have implications for ice shelf basal melt. The onshore transport of warm anomalies at the surface can enter an ice cavity near the surface and initiate shallow melting (Jacobs et al., 1992; Jenkins et al., 2016). Additionally, the simulated presence of CDW and buildup of heat at depth can reach the bottom of the ice shelves and initiate deep melting (Jacobs et al., 1992; Jenkins et al., 2016). Rignot and Jacobs (2002) show that an ocean warming of 0.1°C near the grounding line will increase basal melt of ice shelves by 1 m yr^{-1}. Given the current observed and simulated ice shelf basal melt rates range from 0 to 20 m yr^{-1} (lowest rates in the Ross Sea, highest rates in the Amundsen and Bellingshausen Seas), the CM2.6 shelf region volume average temperature anomaly of 0.56°C would increase basal melt by more than 25%, assuming these anomalies reached the ice-ocean interface (Rignot et al., 2013; Schodlok et al., 2016).

Continued observations of temperature and salinity on the shelf and near the ocean-ice interface of Antarctica will provide essential data to test the ability of eddying climate models to accurately represent this region's small and large-scale dynamics. Advances in climate and ice sheet modeling, such as coupling an interactive ice sheet model with even finer resolution ocean models, will lead to more accurate projections of shelf warming, ice shelf melting, and the global distribution of the associated sea level rise.

Acknowledgments
P. B. Goddard and J. Yin were supported by the National Oceanic and Atmospheric Administration (NOAA) CPO project (NA13OAR4310128), the National Science Foundation award OPP-1513411, and the University of Arizona faculty startup funding. P. B. Goddard was also funded by the University of Arizona Department of Geosciences Paul Martin and Sulzer Scholarships. C. O. Dufour was supported by the National Aeronautics and Space Administration (NASA) under award NNX14AL40G and by the Princeton Environmental Institute (PEI) Grand Challenge initiative. The Southern Ocean Carbon and Climate Observations and Modeling (SOCCOM) project, supported under the National Science Foundation award PLR-1425989, provided a favorable environment to present our work and some travel support for this work. We thank Matthew H. England, Gustavo Marques, and an anonymous reviewer for useful comments that greatly improved this paper. The observational and reanalysis data used in this study can be accessed from the URLs provided in the corresponding figure captions. For all other data requests, please contact Paul Goddard (pgoddard@email.arizona.edu).

References

Aiken, C. M., & England, M. H. (2008). Sensitivity of the present-day climate to freshwater forcing associated with Antarctic sea ice loss. *Journal of Climate*, *21*, 3936–3946. https://doi.org/10.1175/2007JCLI1901.1

Årthun, M., Holland, P. R., Nicholls, K. W., & Feltham, D. L. (2013). Eddy-driven exchange between the open ocean and a sub-ice shelf cavity. *Journal of Physical Oceanography*, *43*(11), 2372–2387. https://doi.org/10.1175/JPO-D-13-0137.1

Bamber, J. L., Riva, R. E. M., Vermeersen, B. L. A., & LeBrocq, A. M. (2009). Reassessment of the potential sea-level rise from a collapse of the West Antarctic Ice Sheet. *Science*, *324*(5929), 901–903. https://doi.org/10.1126/science.1169335

Bintanja, R., van Oldenborgh, G. J., Drijfhout, S. S., Wouters, B., & Katsman, C. A. (2013). Important role for ocean warming and increased ice-shelf melt in Antarctic sea-ice expansion. *Nature Geoscience*, *6*, 376–379. https://doi.org/10.1038/ngeo1767

Christie, F. D. W., Bingham, R. G., Gourmelen, N., Tett, S. F. B., & Muto, A. (2016). Four-decade record of pervasive grounding line retreat along the Bellingshausen margin of West Antarctica. *Geophysical Research Letters*, *43*, 5741–5749. https://doi.org/10.1002/2016GL068972

Cook, A. J., Holland, P. R., Meredith, M. P., Murray, T., Luckman, A., & Vaughan, D. G. (2016). Ocean forcing of glacier retreat in the western Antarctic Peninsula. *Science*, *353*(6296), 283–286. https://doi.org/10.1126/science.aae0017

Danabasoglu, G., Large, W. G., & Briegleb, B. P. (2010). Climate impacts of parameterized Nordic Sea overflows. *Journal of Geophysical Research*, *115*, C11005. https://doi.org/10.1029/2010JC006243

DeConto, R. M., & Pollard, D. (2016). Contribution of Antarctica to past and future sea-level rise. *Nature*, *531*(7596), 591–597. https://doi.org/10.1038/nature17145

Dee, D. P., Uppala, S. M., Simmons, A. J., Berrisford, P., Poli, P., Kobayashi, S., . . . Vitart, F. (2011). The ERA-Interim reanalysis: Configuration and performance of the data assimilation system. *Quarterly Journal of the Royal Meteorological Society*, *137*, 553–597. https://doi.org/10.1002/qj.828

Delworth, T. L., Broccoli, A. J., Rosati, A., Stouffer, R. J., Balaji, V., Beesley, J. A., . . . Zhang, R. (2006). GFDL's CM2 global coupled climate models. Part I: Formulation and simulation characteristics. *Journal of Climate*, *19*(5), 643–674. https://doi.org/101175/JCLI3629.1

Delworth, T. L., Rosati, A., Anderson, W., Adcroft, A. J., Balaji, V., Benson, R., . . . Zhang, R. (2012). Simulated climate and climate change in the GFDL CM2.5 high-resolution coupled climate model. *Journal of Climate*, *25*(8), 2755–2781. https://doi.org/10.1175/JCLI-D-11-00316.1

Depoorter, M. A., Bamber, J. L., Griggs, J. A., Lenaerts, J. T. M., Ligtenberg, S. R. M., van den Broeke, M. R., & Moholdt, G. (2013). Calving fluxes and basal melt rates of Antarctic ice shelves. *Nature*, *502*(7469), 89–92. https://doi.org/10.1038/nature12567

Dinniman, M. S., Klinck, J. M., & Smith, W. O. Jr. (2011). A model study of Circumpolar Deep Water on the West Antarctic Peninsula and Ross Sea continental shelves. *Deep Sea Research Part II: Topical Studies in Oceanography*, *58*(13–16), 1508–1523. https://doi.org/10.1016/j.dsr2.2010.11.013

Dufour, C. O., Griffies, S. M., de Souza, G. F., Frenger, I., Morrison, A. K., Palter, J. B., . . . Slater, R. D. (2015). Role of mesoscale eddies in cross-frontal transport of heat and biogeochemical tracers in the southern ocean. *Journal of Physical Oceanography*, *45*(12), 3057–3081. https://doi.org/10.1175/JPO-D-14-0240.1

Dufour, C. O., Morrison, A. K., Griffies, S. M., Frenger, I., Zanowski, H., & Winton, M. (2017). Preconditioning of the Weddell Sea polynya by the ocean mesoscale and dense water overflows. *Journal of Climate*, *30*, 7719–7737. https://doi.org/10.1175/JCLI-D-16-0586.1

Dupont, T. K., & Alley, R. B. (2005). Assessment of the importance of ice-shelf buttressing to ice-sheet flow. *Geophysical Research Letters*, *32*, L04503. https://doi.org/10.1029/2004GL022024

Flexas, M. M., Schodlok, M. P., Padman, L., Menemenlis, D., & Orsi, A. H. (2015). Role of tides on the formation of the Antarctic Slope Front at the Weddell-Scotia Confluence. *Journal of Geophysical Research: Oceans*, *120*, 3658–3680. https://doi.org/10.1002/2014JC010372

Fox-Kemper, B., Danabasoglu, G., Ferrari, R., Griffies, S. M., Hallberg, R. W., Holland, M. M., . . . Samuels, B. L. (2011). Parameterizations of mixed layer eddies. III: Implementation and impact in global ocean climate simulations. *Ocean Modelling*, *39* (1–2), 61–78. https://doi.org/10.1016/j.ocemod.2010.09.002

Gill, A. E. (1973). Circulation and bottom water production in Weddell Sea. *Deep Sea Research and Oceanographic Abstracts*, *20*(2), 111–140. https://doi.org/10.1016/0011-7471(73)90048-X

Greenbaum, J. S., Blankenship, D. D., Young, D. A., Richter, T. G., Roberts, J. L., Aitken, A. R. A., . . . Siegert, M. J. (2015). Ocean access to a cavity beneath Totten Glacier in East Antarctica. *Nature Geoscience*, *8*(4), 294–298. https://doi.org/10.1038/ngeo2388

Griffies, S. M. (2012). Elements of the Modular Ocean Model (MOM) (Tech. Rep. 7, 618 pp.). NOAA Geophysical Fluid Dynamics Laboratory Ocean Group. Retrieved from http://www.mom-ocean.org/web/docs/project/MOM5_elements.pdf

Griffies, S. M., Winton, M., Anderson, W. G., Benson, R., Delworth, T. L., Dufour, C. O., . . . Zhang, R. (2015). Impacts on ocean heat from transient mesoscale eddies in a hierarchy of climate models. *Journal of Climate*, *28*(3), 952–977. https://doi.org/10.1175/JCLI-D-14-00353.1

Hallberg, R. (2013). Using a resolution function to regulate parameterizations of oceanic mesoscale eddy effects. *Ocean Modelling*, *72*, 92–103. https://doi.org/10.1016/j.ocemod.2013.08.007

Hattermann, T., Smedsrud, L. H., Nøst, O. A., Lilly, J. M., & Galton-Fenzi, B. K. (2014). Eddy-resolving simulations of the Fimbul Ice cavity circulation: Basal melting and exchange with open ocean. *Ocean Modelling*, *82*(28), 28–44. https://doi.org/10.1016/j.ocemod.2014.07.004

Heuze, C., Heywood, K. J., Stevens, D. P., & Ridley, J. K. (2013). Southern Ocean bottom water characteristics in CMIP5 models. *Geophysical Research Letters*, *40*, 1409–1414. https://doi.org/10.1002/grl.50287

IOC, SCOR, & IAPSO. (2010). The international thermodynamic equation of seawater – 2010: Calculation and use of thermodynamic properties. In *Intergovernmental Oceanographic Commission manuals and guides 56* (196 pp.). UNESCO. Retrieved from http://www.teos-10.org/TEOS-10_Manual.pdf

Isachsen, P. E. (2011). Baroclinic instability and eddy tracer transport across sloping bottom topography: How well does a modified Eady model do in primitive equation simulations? *Ocean Modelling*, *39*, 183–199. https://doi.org/10.1016/j.ocemod.2010.09.007

Jacobs, S. S. (1991). On the nature and significance of the Antarctic Slope Front. *Marine Chemistry*, *35*(1–4), 9–24. https://doi.org/10.1016/S0304-4203(09)90005-6

Jacobs, S. S., Hellmer, H. H., Doake, C. S. M., Jenkins, A., & Frolich, R. M. (1992). Melting of ice shelves and the mass balance of Antarctica. *Journal of Glaciology*, *38*(130), 375–387.

Jacobs, S. S., Hellmer, H. H., & Jenkins, A. (1996). Antarctic ice sheet melting in the Southeast Pacific. *Geophysical Research Letters*, *23*(9), 957–960. https://doi.org/10.1029/96GL00723

Jenkins, A., Dutrieux, P., Jacobs, S., Steig, E. J., Gudmundsson, G. H., Smith, J., & Heywood, K. J. (2016). Decadal ocean forcing and Antarctic ice sheet response: Lessons from the Amundsen Sea. *Oceanography*, *29*, 106–117. https://doi.org/10.5670/oceanog.2016.103

Kalnay, E., Kanamitsu, M., Kistler, R., Collins, W., Deaven, D., Gandin, L., . . . Wang, J. (1996). The NCEP/NCAR 40-year reanalysis project. *Bulletin of the American Meteorological Society*, *77*, 437–470. https://doi.org/10.1175/1520-0477(1996)077<0437:TNYRP>2.0.CO;2

Large, W. G., McWilliams, J. C., & Doney, S. C. (1994). Oceanic vertical mixing: A review and a model with a nonlocal boundary layer parameterization. *Reviews of Geophysics*, *32*(4), 363–403. https://doi.org/10.1029/94RG01872

Lythe, M. B., Vaughan, D. G., & BEDMAP Consortium. (2001). BEDMAP: A new ice thickness and subglacial topographic model of Antarctica. *Journal of Geophysical Research*, *106*(B6), 11,335–11,351. https://doi.org/10.1029/2000JB900449

MacCready, P., & Rhines, P. B. (1993). Slippery bottom boundary layers on a slope. *Journal of Physical Oceanography*, *23*, 5–22. https://doi.org/10.1175/1520-0485(1993)023<0005:SBBLOA>2.0.CO;2

Marshall, G. J. (2003). Trends in the southern annular mode from observations and reanalyses. *Journal of Climate*, *16*, 4134–4143. https://doi.org/10.1175/1520-0442(2003)016<4134:TITSAM>2.0.CO;2

Martinson, D. G., Stammerjohn, S. E., Iannuzzi, R. A., Smith, R. C., & Vernet, M. (2008). Western Antarctic Peninsula physical oceanography and spatio-temporal variability. *Deep Sea Research Part II: Topical Studies in Oceanography*, *55*(18–19), 1964–1987. https://doi.org/10.1016/j.dsr2.2008.04.038

Meinshausen, M., Smith, S. J., Calvin, K., Daniel, J. S., Kainuma, M. L. T., Lamarque, J.-F., . . . van Vuuren, D. P. P. (2011). The RCP greenhouse gas concentrations and their extensions from 1765 to 2300. *Climatic Change*, *109*(1–2), 213–241. https://doi.org/10.1007/s10584-011-0156-z

Moffat, C., Owens, B., & Beardsley, R. C. (2009). On the characteristics of Circumpolar Deep Water intrusions to the west Antarctic Peninsula. *Journal of Geophysical Research*, *114*, C05017. https://doi.org/10.1029/2008JC004955

Morrison, A. K., England, M. H., & Hogg, A. M. (2015). Response of Southern Ocean convection and abyssal overturning to surface buoyancy perturbations. *Journal of Climate*, *28*, 4263–4278. https://doi.org/10.1175/JCLI-D-14-00110.1

Newsom, E. R., Bitz, C. M., Bryan, F. O., Abernathey, R., & Gent, P. R. (2016). Southern Ocean deep circulation and heat uptake in a high-resolution climate model. *Journal of Climate*, *29*, 2597–2619. https://doi.org/10.1175/JCLI-D-15-0513.1

Nøst, O. A., Biuw, M., Tverdrup, V., Lydersen, C., Hattermann, T., Zhou, Q., . . . Kovacs, K. M. (2011). Eddy overturning of the Antarctic Slope Front controls glacial melting in the Eastern Weddell Sea. *Journal of Geophysical Research*, *116*, C11014. https://doi.org/1029/2011JC006965

Obase, T., Abe-Ouchi, A., Kusahara, K., Hasumi, H., & Ohgaito, R. (2017). Responses of basal melting of the Antarctic ice shelves to the climate forcing of the Last Glacial Maximum and CO_2 doubling. *Journal of Climate*, *30*, 3473–3497. https://doi.org/10.1175/JCLI-D-15-0908.1

Orsi, A. H., Johnson, G. C., & Bullister, J. L. (1999). Circulation, mixing, and production of Antarctic Bottom Water. *Progress in Oceanography*, *43*, 55–109. https://doi.org/10.1016/S0079-6611(99)00004-X

Payne, A. J., Vieli, A., Shepherd, A. P., Wingham, D. J., & Rignot, E. (2004). Recent dramatic thinning of largest West Antarctic ice stream triggered by oceans, *Geophysical Research Letters*, *31*, L23401. https://doi.org/10.1029/2004GL021284

Pritchard, H. D., Ligtenberg, S. R. M., Fricker, H. A., Vaughan, D. G., van den Broeke, M. R., & Padman, L. (2012). Antarctic ice-sheet loss driven by basal melting of ice shelves. *Nature*, *484*(7395), 502–505. https://doi.org/10.1038/nature10968

Rignot, E., Bamber, J. L., van den Broeke, M. R., Davis, C., Li, Y., van Ve Berg, W. J., & van Meijgaard, E. (2008). Recent Antarctic ice mass loss from radar interferometry and regional climate modeling. *Nature Geoscience*, *1*(2), 106–110. https://doi.org/10.1038/ngeo102

Rignot, E., & Jacobs, S. S. (2002). Rapid bottom melting widespread near Antarctic ice sheet grounding line. *Science*, *296*(5575), 2020–2023. https://doi.org/10.1126/science.1070942

Rignot, E., Jacobs, S., Mouginot, J., & Scheuchl, B. (2013). Ice-shelf melting around Antarctica. *Science*, *341*(6143), 266–270. https://doi.org/10.1126/science.1235798

Rintoul, S. R., & Naveira Garabato, A. C. (2013). Dynamics of the Southern Ocean circulation. In G. Siedler et al. (Eds.), *Ocean circulation and climate, a 21st century perspective*, (2nd ed., Vol. 103, pp. 471–492). Oxford, UK: Academic Press.

Schodlok, M. P., Menemenlis, D., & Rignot, E. (2016). Ice shelf basal melt rates around Antarctica from simulations and observations. *Journal of Geophysical Research: Oceans*, *121*, 1085–1109. https://doi.org/10.1002/2015JC011117

Shepherd, A., Wingham, D., & Rignot, E. (2004). Warm ocean is eroding West Antarctic Ice Sheet. *Geophysical Research Letters*, *31*, L23402. https://doi.org/10.1029/2004GL021106

Sparrow, M., P. Chapman, & Gould, J. (Eds.) (2011). *2005 The World Ocean Circulation Experiment (WOCE) hydrographic atlas series* (4 volumes). Southampton, UK: International WOCE Project Office.

Spence, P., Griffies, S. M., England, M. H., Hogg, A. M., Saenko, O. A., & Jourdain, N. C. (2014). Rapid subsurface warming and circulation changes of Antarctic coastal waters by poleward shifting winds. *Geophysical Research Letters*, *41*, 4601–4610. https://doi.org/10.1002/2014GL060613

Spence, P., Holmes, R. M., Hogg, A. M., Griffies, S. M., Stewart, K. D., & England, M. H. (2017). Localized rapid warming of West Antarctic subsurface waters by remote winds. *Nature Climate Change*, *7*, 595–603. https://doi.org/10.1038/nclimate3335

Stevens, D. P., & Killworth, P. D. (1992). The distribution of kinetic energy in the Southern Ocean: A comparison between observations and an eddy resolving general circulation model. *Philosophical Transactions of the Royal Society of London, Series B: Biological Sciences*, *338B*, 251–257.

Stewart, A. L., & Thompson, A. F. (2015). Eddy-mediated transport of warm Circumpolar Deep Water across the Antarctic Shelf Break. *Geophysical Research Letters*, *42*, 432–440. https://doi.org/10.1002/2014GL062281

Stewart, A. L., & Thompson, A. F. (2016). Eddy generation and jet formation via dense water outflows across the Antarctic continental slope. *Journal of Physical Oceanography*, *46*, 3729–3750. https://doi.org/10.1175/JPO-D-16-0145.1

St-Laurent, P., Klinck, J. M., & Dinniman, M. S. (2013). On the role of coastal troughs in the circulation of warm Circumpolar Deep Water on Antarctic shelves. *Journal of Physical Oceanography*, *43*(1), 51–64. https://doi.org/10.1175/JPO-D-11-0237.1

Swart, N. C., & Fyfe, J. C. (2012). Observed and simulated changes in the southern hemisphere surface westerly wind-stress. *Geophysical Research Letters*, *39*, L16711. https://doi.org/10.1029/2012GL052810

Thompson, D. W. J., & Solomon, S. (2002). Interpretation of recent southern hemisphere climate change. *Science*, *296*, 895–899. https://doi.org/10.1126/science.1069270

Timmermann, R., & Hellmer, H. H. (2013). Southern Ocean warming and increased ice shelf basal melting in the twenty-first and twenty-second centuries based on coupled ice-ocean finite-element modelling. *Ocean Dynamics*, *63*, 1011–1026. https://doi.org/10.1007/s10236-013-0642-0

van Vuuren, D. P., Edmonds, J., Kainuma, M., Riahi, K., Thomson, A., Hibbard, K., . . . Rose, S. K. (2011). The representative concentration pathways: An overview. *Climatic Change*, *109*(1–2), 5–31. https://doi.org/10.1007/s10584-011-0148-z

Wåhlin, A. K., Muench, R. D., Arneborg, L., Björk, G., Ha, H. K., Lee, S. H., & Alsén, H. (2012). Some implications of Ekman layer dynamics for cross-shelf exchange in the Amundsen Sea. *Journal of Physical Oceanography*, *42*, 1461–1474. https://doi.org/10.1175/JPO-D-11-041.1

Whitworth, T., Orsi, A. H., Kim, S. J., Nowlin, W. D., & Locarnini, R. A. (1998). Water masses and mixing near the Antarctic Slope Front. In S. S. Jacobs & R. F. Weiss (Eds.), *Ocean, ice, and atmosphere: Interactions at the Antarctic continental margins, Antarctic Research Series* (Vol. 75, pp. 1–27). Washington, DC: AGU. https://doi.org/10.1029/AR075p0001

Winton, M., Hallberg, R., & Gnanadesikan, A. (1998). Simulation of density-driven frictional downslope flow in z-coordinate ocean models. *Journal of Physical Oceanography*, *28*, 2163–2173. https://doi.org/10.1175/1520-0485(1998)028<2163:SODDFD>2.0.CO;2

Yin, J., Overpeck, J. T., Griffies, S. M., Hu, A., Russell, J. L., & Stouffer, R. J. (2011). Different magnitudes of projected subsurface ocean warming around Greenland and Antarctica. *Nature Geoscience*, *4*, 524–528. https://doi.org/10.1038/ngeo1189